Title

Condensation of PRPP amidotransferase by phase separation promotes *de novo* purine synthesis through intermolecular intermediate channeling in yeast

Masak Takaine[1,2], Rikuri Morita[3], Yuto Yoshinari[4], and Takashi Nishimura[4]

[1]GIAR and [2]IMCR, Gunma University, Maebashi, Japan; [3]Center for Computational Sciences, University of Tsukuba, Ibaraki, Japan; [4]Laboratory of Metabolic Regulation and Genetics, Institute for Molecular and Cellular Regulation, Gunma University, Maebashi, Gunma 371-8512 Japan

Keywords: *de novo* purine synthesis, PRPP amidotransferase (PPAT), phase separation, TORC1, yeast

*Correspondence should be addressed to: masaktakaine@gunma-u.ac.jp (M.T.)

Highlights

- PRPP amidotransferase (PPAT) in budding yeast forms dynamic intracellular condensates in response to environmental purine deprivation.
- Ribosome crowding in the cytoplasm, induced by TORC1, drives the assembly of PPAT condensates.
- The purified PPAT protein alone condensates into submicron-sized particles *in vitro* under molecular crowding conditions.
- Purine nucleotides inhibit the self-assembly of PPAT, while PRPP promotes this process and counteracts the inhibition.
- The condensation of PPAT facilitates the intermolecular channeling of intermediates, thereby enhancing *de novo* purine synthesis.

Summary

De novo purine synthesis (DPS) is up-regulated under conditions of high purine demand to ensure the production of genetic materials and chemical energy, thereby supporting cell proliferation. However, the regulatory mechanisms governing DPS remain largely unclear. We herein show that PRPP amidotransferase (PPAT), the rate-limiting enzyme in DPS, forms dynamic and motile condensates in *Saccharomyces cerevisiae* cells under a purine-depleted environment. The formation of condensates requires phase separation, which is driven by target of rapamycin complex 1 (TORC1)-induced ribosome biosynthesis. The self-assembly of PPAT molecules facilitates condensate formation, with intracellular PRPP and purine nucleotides both regulating this self-assembly. Moreover, molecular dynamics simulations suggest that clustering-mediated PPAT activation occurs through intermolecular substrate channeling. Cells unable to form PPAT condensates exhibit growth defects, highlighting the physiological importance of condensation. These results suggest that PPAT condensation is an adaptive mechanism that regulates DPS in response to both TORC1 activity and cellular purine demands.

Introduction

Purine nucleotides and their derivatives play crucial roles in many cellular processes, making them essential metabolites for all living organisms. The purine nucleotide triphosphates, ATP and GTP, act as cellular energy currencies. In addition, purine metabolites are integrated into genetic materials, such as DNA and RNA, and into coenzymes, including NAD and coenzyme A. Purine nucleotides are synthesized through either salvage or *de novo* pathways. Under normal conditions, cells primarily synthesize the majority of purine nucleotides via the salvage pathway by adding phosphoribosyl pyrophosphate (PRPP), derived from the pentose phosphate pathway, to purine bases, which are often imported from outside the cell. Since at least one of the two pathways is required for purine synthesis, they provide a fail-safe mechanism for each other.

The *de novo* purine biosynthetic pathway consists of ten highly conserved sequential chemical reactions facilitated by six enzymes that convert PRPP to inosine 5′-monophosphate (IMP). IMP is then converted into adenosine 5′-monophosphate (AMP) or guanine 5′-monophosphate (GMP) through two branched paths. Among these enzymes, PRPP amidotransferase (PPAT) (EC 2.4.2.14) is the rate-limiting enzyme and plays a pivotal role in the regulation of *de novo* purine synthesis. PPAT catalyzes the initial step of the *de novo* pathway, namely, the transfer of amino groups from glutamine to PRPP to produce 5-phosphoribosylamine (PRA) (eq. 1). This reaction is further divided into two half-reactions: the release of ammonia (NH_3) from glutamine (eq. 2) and the ligation of NH_3 with PRPP (eq. 3). PPAT is a bifunctional enzyme with two catalytic domains, possessing an N-terminal glutamine amidotransferase (GATase) domain that catalyzes the former reaction, and a C-terminal phosphoribosyltransferase (PRTase) domain for the latter.

$$\mathbf{PRPP + glutamine + H_2O \rightarrow PRA + glutamate + PP_i} \quad \text{(eq. 1)}$$

$$\mathbf{glutamine + H_2O \rightarrow NH_3 + glutamate} \quad \text{(eq. 2)}$$

$$\mathbf{PRPP + NH_3 \rightarrow PRA + PP_i} \quad \text{(eq. 3)}$$

While the biochemical properties of each enzyme involved in purine synthesis have been extensively examined, the regulation of *de novo* purine synthesis within cells remains unclear. In bacterial and mammalian cells, when extracellular purine bases are available, purine nucleotides are preferentially synthesized by recycling bases through the salvage pathway, while the *de novo* pathway is strongly down-regulated[1 2]. Conversely, under conditions of purine deprivation or high purine demand (*e.g.*, in actively proliferating cells), the *de novo* pathway is activated to provide sufficient levels of purine

nucleotides[3]. Although the mechanisms underlying these regulatory processes have not yet been elucidated in detail, cells appear to limit the use of the *de novo* pathway in order to conserve energy and resources because the generation of each IMP requires up to five ATP and four amino acids.

The enzyme activity of PPAT is subject to feedback inhibition by the end products of the *de novo* pathway, such as AMP and GMP [4-6]. This inhibition is considered to play a role in both suppressing *de novo* purine synthesis in the presence of salvageable extracellular purine bases and activating it during purine starvation [4]. However, millimolar levels of AMP or GMP are required to inhibit PPAT catalytic activity[4, 6, 7], whereas intracellular concentrations of these nucleotides are markedly lower [8], raising questions about the physiological relevance of this feedback inhibition. Other regulatory layers of PPAT activity, such as post-translational modifications and intracellular signaling, may also play a role, but have yet to be investigated.

Emerging evidence suggests that many metabolic enzymes, including PPAT, form condensates in response to external stimuli in order to regulate cellular metabolism [9]. For example, the pyruvate kinase Cdc19 in budding yeast reversibly aggregates into large foci upon glucose starvation and heat shock [10, 11]. This aggregation protects Cdc19 from stress-induced degradation and inactivates it, both of which are crucial for the efficient formation of stress granules and cell regrowth after stress. Similarly, PPAT reversibly localizes to cytoplasmic condensates upon the depletion of extracellular purine bases in budding yeast and HeLa cells [12, 13]. Recent studies indicated that in HeLa cells, PPAT also colocalized with other enzymes involved in *de novo* purine synthesis within a multi-enzyme cellular complex known as a purinosome, which appeared to enhance pathway flux near mitochondria [14]. However, the mechanisms regulating the formation of PPAT condensates and its physiological significance remain unclear.

We herein demonstrate that PPAT forms dynamic intracellular condensates through phase separation in budding yeast cells in the absence of external purine bases. Active ribosome synthesis promoted by target of rapamycin complex 1 (TORC1) is crucial for the molecular crowding that drives the phase transition. An *in vitro* analysis showed that the self-assembly of PPAT alone is sufficient for condensate formation, which is inhibited by purine nucleotides. Moreover, increased intracellular PRPP promotes the condensation of PPAT, opposing the inhibitory effects of purine nucleotides. Molecular dynamics (MD) simulations suggest the condensation-dependent activation of the enzyme by intermolecular NH_3 channeling. Consistent with these results, PPAT condensates play a vital role in *de novo* purine synthesis to ensure cell proliferation. Collectively, we propose that PPAT condensation by phase transition is a rapid regulatory mechanism for *de novo*

116 purine synthesis in response to both TORC1 activity and available purine bases.

Results

The yeast PPAT Ade4 concentrates in fine particles

Previous semi-comprehensive analyses revealed that the budding yeast PPAT Ade4 formed cytoplasmic foci in response to environmental purine bases[12, 15]. However, the dynamics of the assembly and disassembly of Ade4 foci, their physical properties, and the mechanisms underlying the formation of foci remain unclear. Therefore, we reexamined Ade4 foci using a cell biological approach. In the present study, adenine was used as a representative purine base because of its high solubility in medium and its role as a precursor for both AMP and GMP through reverse conversion from AMP to IMP (Fig. 1A). We visualized the localization of the Ade4 protein by tagging the chromosomal *ADE4* gene with a yeast codon-optimized GFP (hereafter referred to as GFP). As demonstrated in previous studies [12, 15], Ade4-GFP showed a large focus in cells transferred into medium lacking purine bases, but not in the presence of adenine (Fig. 1B). Unexpectedly, Ade4 tagged with a GFP bearing the monomeric mutation A206K[16] (Ade4-mGFP) appeared as numerous fine dim dots under the same conditions (Fig. 1B). Consistently, Ade4 tagged with monomeric NeonGreen (Ade4-mNG) formed fine particles with markedly higher fluorescence intensities (Fig. 1B-C). Ade4 tagged with the monomeric red fluorescent protein mKate2 (Ade4-mKate2) showed similar particle localization (Fig. S1A). Therefore, we conclude that Ade4-GFP concentrates into 1-2 foci due to GFP dimerization.

Z-stack imaging revealed that Ade4-mNG particles localized throughout the cytoplasm (Fig. 1D). Time-lapse imaging further demonstrated that these particles were dynamic structures: they assembled within 40 min after the depletion of extracellular adenine (Figs. 1E, G and S1B, and Movies S1-S3) and disassembled within 10 min after adenine supplementation (Figs. 1F, H and S1C, and Movies S4-S6). Closer time-lapse imaging indicated the high motility of particles: they moved freely in three dimensions and repeatedly moved in and out of the focal plane within seconds (Figs. 1I-K and S1D-F, and Movie S7). These results suggest that Ade4 forms dynamic and motile particles in response to the availability of purines.

In subsequent experiments, we primarily focused on Ade4-mNG particles to elucidate the molecular mechanisms regulating Ade4 condensation. We also examined the assembly of Ade4-GFP foci due to their similar properties to Ade4-mNG particles and their suitability for high-content imaging because of their higher brightness.

Ade4 particles have liquid-like properties

The reversible assembly and dynamic nature of Ade4-mNG particles prompted us to

153 hypothesize that they are liquid-like assemblies rather than static, solid-like aggregates.
154 Therefore, we treated cells containing Ade4-mNG with 1,6-hexanediol, an aliphatic
155 alcohol that dissolves various intracellular membrane-less structures [17]. The
156 permeabilization of yeast cells with digitonin did not affect the assembly of Ade4-mNG
157 particles, whereas particles exposed to 10% 1,6-hexanediol plus digitonin significantly
158 disassembled within 10 min, confirming their liquid-like properties (Fig. 2A-B).
159 Previous studies highlighted the role of an intrinsically disordered region (IDR) in
160 the formation of intracellular membrane-less structures[18]. We analyzed the amino acid
161 sequences of Ade4 and other PPATs using the DISOPRED algorithm[19], a neural network-
162 based method that predicts IDRs. We identified an IDR at the C terminus of Ade4 (Fig.
163 2C). The presence of the IDR was highly conserved across Ade4 homologues in
164 Ascomycota and all fungi (Fig. S2A), as well as in PPATs from other kingdoms, including
165 bacteria and mammals (Fig. S2B). However, the amino acid sequences of IDRs varied
166 across species, even among yeasts (Fig. S2C-D). An Ade4 mutant lacking the IDR,
167 Ade4ΔIDR-mNG, was incapable of forming punctate structures, suggesting the necessity
168 of the IDR for Ade4 particle assembly (Fig. 2D). Collectively, these results suggest that
169 Ade4 molecules condensate into fine particles through IDR-dependent phase separation.
170
171 Formation of Ade4 condensates requires active TORC1 and ribosome biogenesis
172 We examined the factors required for phase separation, which facilitates the assembly
173 of Ade4 condensates. Recent studies suggested that TORC1 controlled phase separation
174 in the cytoplasm of both yeast and mammalian cells by modulating ribosome crowding[20].
175 Therefore, we investigated the role of TORC1 in the formation of Ade4 condensates. In
176 cells, rapamycin binds to FKBP12, forming a complex that effectively inhibits TORC1[21].
177 The addition of rapamycin suppressed the assembly of Ade4-GFP foci in wild-type cells,
178 but not in cells lacking Fpr1 (budding yeast FKBP1) (Fig. 2E). Similarly, rapamycin
179 significantly inhibited the assembly of Ade4-mNG condensates in wild-type cells (Fig.
180 2F-G). These results indicate that TORC1 activity is essential for the formation of Ade4
181 condensates.
182 To further delineate the TORC1-related factors responsible for Ade4 condensate
183 formation, we examined Ade4-GFP foci in 37 single-gene deletion mutants, each lacking
184 one of the 17 upstream regulators, the 17 downstream effectors of TORC1 signaling, or
185 3 genes of interest (Fig. S3A-B). Consistent with the inhibitory effects of rapamycin, the
186 assembly of Ade4-GFP foci was typically reduced in mutants of the upstream activators
187 of TORC1 signaling (such as the Pib2 or EGO complex). In contrast, most of the
188 downstream effectors of TORC1 signaling exerted negligible or no effects on the

189 formation of Ade4-GFP foci. However, the formation of Ade4-GFP foci and Ade4-mNG
190 condensates was significantly suppressed in *sfp1*Δ and *sit4*Δ cells (Figs. 2H-I and S3A-
191 B).
192 Sfp1 is a transcriptional activator that regulates the expression of ribosomal protein
193 and ribosome biogenesis genes [22]. Sit4 is a subunit of type 2A protein phosphatase, the
194 activity of which is controlled by TORC1 [23]. Both have been implicated in cytoplasmic
195 crowding through ribosome biogenesis downstream of TORC1 [20, 24, 25]. Therefore, we
196 evaluated the importance of ribosome synthesis on Ade4 condensate formation.
197 Diazaborine specifically inhibits the maturation of the 60S ribosomal subunit and reduces
198 the level of the 60S subunit in yeast cells [26]. Treatment with diazaborine strongly
199 suppressed the formation of Ade4-GFP foci and Ade4-mNG condensates, indicating that
200 active synthesis of the ribosomal 60S subunit was required for the assembly of these
201 condensates (Figs. 2J and S3C-D). Collectively, these results suggest that
202 macromolecular crowding of the cytoplasm, driven by TORC1-mediated ribosome
203 synthesis, is a primary mechanism facilitating the phase separation required for Ade4
204 condensation.
205
206 Ade4 protein condensates into particles under molecular crowding conditions *in*
207 *vitro*
208 Two hypotheses have been proposed for the molecular mechanisms regulating the
209 assembly of Ade4 condensates. The first hypothesis suggests that Ade4 alone is sufficient
210 for condensate formation, while the second posits that additional cellular components,
211 such as proteins, lipids, and organelles, are required for Ade4 to condensate into particles.
212 To distinguish between these possibilities, we investigated the properties of the purified
213 Ade4 protein *in vitro*. Previous attempts to express Ade4 in its active form in bacteria
214 were unsuccessful [27], prompting us to purify Ade4-mNG directly from budding yeast cells
215 (Fig. S4A). Based on the findings of 20 quantitative proteomic studies, the intracellular
216 concentrations of Ade4 were estimated to be approximately 0.5 μM (Fig. S5). In our *in*
217 *vitro* assays, we selected concentrations of Ade4-mNG that were close to or slightly lower
218 than this estimated value.
219 Under physiological ionic conditions (150 mM NaCl and 4 mM $MgCl_2$, pH 7.5),
220 purified Ade4-mNG dispersed homogenously, showing no signs of condensate formation
221 ("0%" in Fig. 3A). We then examined the effects of macromolecular crowding using
222 polyethylene glycol (PEG) as a crowding agent. The addition of PEG8000 led to the
223 formation of sub-micron-sized particles of Ade4-mNG in a concentration-dependent
224 manner; significant amounts of particles formed at concentrations higher than 10% PEG

225 (Fig. 3A-C). Controls with the mNG protein alone did not form particles in 10% PEG
226 (Fig. S4B). We also investigated the effects of different sizes of PEG and found that Ade4-
227 mNG self-assembled into particles in the presence of PEG molecular weights higher than
228 4 kDa (Fig. S4C-E). Consistent with this size dependency, other crowding agents, such
229 as 2% lysozyme (MW: 14 kDa) and Ficoll-400 (MW: 400 kDa), also induced the
230 assembly of Ade4-mNG particles (Fig. S4F). These results suggest that Ade4 self-
231 assembles into sub-micron particles that are similar in size to intracellular condensates
232 under macromolecular crowding conditions.
233 We also investigated the role of phase separation in the self-assembly of Ade4-mNG
234 *in vitro*. In the presence of 1,6-hexanediol, the mean fluorescence intensity and total mass
235 of Ade4-mNG particles were both markedly reduced (Fig. 3D-F). Consistently, the
236 deletion of IDR from Ade4 markedly reduced condensate formation; however, the
237 Ade4ΔIDR-mNG protein still formed visible particles (Fig. 3G-I). These results suggest
238 that while Ade4 molecules form condensates independent of the C-terminal IDR moiety,
239 phase separation is responsible for the complete assembly of Ade4 particles *in vitro*.
240

241 Metabolomics analysis of budding yeast cells grown in the absence and presence
242 of adenine

243 We investigated the mechanisms by which intracellular Ade4 condensates assemble
244 in response to environmental purine deprivation. Nutrients such as amino acids and
245 glucose typically regulate the activity of TORC1 [28]. However, environmental purine bases,
246 including adenine, do not affect TORC1 activity in mammalian cells [29, 30]. Based on these
247 findings, TORC1-mediated macromolecular crowding, which drives Ade4 condensate
248 assembly, appears to be independent of extracellular purine base levels. Therefore, there
249 may be additional layers of regulation that either suppress or promote condensate
250 formation based on the availability of environmental purines. We hypothesized that
251 metabolites related to the incorporated purine bases regulate the assembly of Ade4
252 condensates.
253 To identify these functional metabolites, we conducted a comprehensive
254 metabolomics analysis using liquid chromatography-tandem mass spectrometry. Wild-
255 type cells were cultured in the absence or presence of adenine for 1, 7, and >24 h and
256 were then collected for metabolic profiling (Fig. 4A). A supervised classification method,
257 a sparse partial least squares discriminant analysis (PLS-DA), demonstrated that samples
258 were distinctly separated based on the presence of environmental adenine and the duration
259 of exposure to adenine (Fig. 4B and Supplementary Data S1). A one-way analysis of
260 variance (ANOVA) identified 56 metabolites whose concentrations were significantly

261 affected by adenine (Fig. 4C and Supplementary Data S2). The metabolic profile changed
262 over the duration of adenine exposure, indicating both short- and long-term responses
263 (Fig. 4B-C). Intracellular concentrations of adenine increased more than five-fold within
264 1 h of the addition of adenine (Fig. 4D and Supplementary Data S3). A correlation
265 analysis revealed that the concentrations of several metabolites, such as hypoxanthine,
266 inosine, and deoxynucleotides, positively correlated with the change in intracellular
267 adenine (Fig. 4E). Among them, hypoxanthine, which is directly converted from adenine,
268 showed the greatest increase after adenine supplementation, and remained elevated (Fig.
269 4D). Meanwhile, purine nucleotides and their derivatives slightly increased in the
270 presence of adenine, with only some of these changes being significant.
271

272 ## Intracellular derivatives of purine nucleotides regulate the formation of Ade4
273 condensates

274 Since intracellular concentrations of adenine and hypoxanthine rapidly and
275 significantly increased upon the addition of adenine, we speculated that these metabolites
276 may suppress the formation of intracellular Ade4 condensates. However, these purine
277 bases were converted to various metabolites after active uptake into cells through the
278 purine-cytosine permease Fcy2[31] (Fig. 5A). Therefore, we used mutant strains to clarify
279 whether adenine and hypoxanthine suppressed Ade4 condensate formation. When wild-
280 type cells were treated with medium containing either adenine or hypoxanthine, Ade4-
281 GFP foci were completely disassembled (Fig. 5B-E, wt), indicating that hypoxanthine
282 acted as an adenine substitute. In *aah1*Δ*apt1*Δ cells, in which incorporated adenine was
283 not metabolized further, the addition of adenine failed to disassemble Ade4 foci, whereas
284 that of hypoxanthine completely disassembled foci (Fig. 5B-C), suggesting that adenine
285 itself did not affect Ade4 condensates. Conversely, in *hpt1*Δ cells, in which incorporated
286 hypoxanthine was not metabolized further, the addition of hypoxanthine failed to
287 disassemble Ade4 foci (Fig. 5B, D), indicating that hypoxanthine itself also did not affect
288 Ade4 condensates. Notably, adenine failed to completely disassemble Ade4-GFP foci in
289 *hpt1*Δ cells, suggesting that adenine affected wild-type cells primarily through its
290 metabolic conversion to hypoxanthine.
291 We also investigated the effects of purine nucleotide metabolism on condensate
292 disassembly. In *ade12*Δ cells, in which IMP was not converted to AMP via
293 adenylosuccinate (S-AMP), the addition of hypoxanthine failed to disassemble Ade4 foci,
294 whereas adenine moderately decreased foci (Fig. 5B, E). The inhibition of Ade12 by
295 alanosine, a specific inhibitor of adenylosuccinate synthetase [32], produced similar results
296 (Fig. S7A-C). Therefore, we conclude that the anabolism of external purine bases is

297 required to regulate the assembly of Ade4 condensates.
298
299 ## Purine nucleotides attenuate the assembly of Ade4 condensates *in vitro*
300 The results of our genetic analyses suggest that AMP and related purine nucleotide
301 derivatives play a vital role as functional metabolites that regulate the formation of Ade4
302 condensates. To directly test this possibility, we examined the inhibitory effects of purine
303 nucleotides on the *in vitro* assembly of Ade4-mNG condensates. In the presence of GMP,
304 AMP, ADP, and ATP, the condensation of Ade4-mNG was significantly reduced (Fig. 6A-
305 B and Fig. S8C). AMP, ADP, and ATP were more effective than GMP, while S-AMP had
306 no significant effect. Concentrations higher than 250 μM of AMP, ADP, or ATP were
307 required to achieve maximal inhibitory effects, whereas the inhibitory effects of GMP
308 plateaued at 100 μM (Fig. 6C and Fig. S8D-F). Consistent with our *in vivo* results (Fig.
309 5), adenine did not affect the *in vitro* condensation of Ade4 (Fig. S8A-B). Similarly, the
310 ribose-bound hypoxanthine derivatives, inosine and deoxyinosine (dI), had no impact on
311 Ade4 condensation (Fig. S8A-B). S-adenosylhomocysteine (SAH), a derivative of S-
312 adenosylmethionine, exerted approximately one-third the inhibitory effect of AMP (Fig.
313 S8G-H). Importantly, AMP also inhibited the condensation of Ade4ΔIDR-mNG (Fig. 6D).
314 These results suggest that purine nucleotides, including AMP, ADP, ATP, and GMP,
315 suppress the condensation of Ade4 molecules by inhibiting IDR-independent self-
316 assembly.
317
318 ## PRPP facilitates the assembly of Ade4 condensates *in vitro* and *in vivo*
319 The inhibitory effects of purine nucleotides on the *in vitro* formation of Ade4
320 condensates led us to hypothesize that these nucleotides may similarly regulate the
321 formation of intracellular Ade4 condensates. However, the limited extent of these
322 inhibitory effects suggested the existence of additional regulatory factors that promote
323 the condensation of Ade4. The intracellular concentrations of these factors may decrease
324 with adenine supplementation and increase when adenine is absent. Our correlation
325 analysis identified several metabolites whose changes inversely correlated with
326 intracellular adenine levels (Fig. 4E). Among them, we focused on IMP, which is directly
327 synthesized from hypoxanthine, and PRPP, which directly interacts with Ade4 as a
328 substrate (Fig. 4D). We found that IMP did not affect the assembly of Ade4 condensates
329 *in vitro*, even at concentrations that were higher than those in yeast cells [8] (Fig. S9A-B).
330 In contrast, PRPP concentrations higher than 50 μM significantly increased the mean
331 fluorescence intensity and total mass of *in vitro* Ade4 condensates under 10% PEG
332 conditions (Figs. 7A and S10A). Quantitative analyses revealed that adenine

333 supplementation reduced intracellular PRPP levels from approximately 30 μM to less
334 than 10 μM (Fig. S6B), guiding our selection of PRPP concentrations within the range of
335 10–200 μM for subsequent assays. Notably, the promoting effects of PRPP were more
336 evident at lower PEG concentrations, at which Ade4 condensates rarely formed; the
337 addition of 100 μM PRPP enabled the formation of Ade4 condensates in 5% and 7.5%
338 PEG (Fig. 7B-C and S10B-C). These results suggest that PRPP promotes and augments
339 the assembly of Ade4 condensates *in vitro*. Furthermore, the inhibitory effect of 1 mM
340 AMP on Ade4 condensation was effectively counteracted by PRPP at concentrations
341 higher than 50 μM, with this effect being more pronounced in 7.5% PEG than in 10%
342 PEG (Fig. 7D, E and S10D), suggesting that PRPP antagonizes the inhibitory effect of
343 AMP.

344 We then examined the effects of PRPP on the formation of cellular Ade4 condensates.
345 The 13-residue PRPP binding motif at the catalytic site is well conserved among PPATs
346 of various species, including budding yeast, with two adjacent aspartic acids that are
347 crucial for PRPP binding [33] (Fig. S10E). A structural analysis of *E. coli* PPAT showed that
348 these aspartic acids formed hydrogen bonds with carbocyclic PRPP (cPRPP), a stable
349 analog of PRPP [34] (Fig. 7F). This motif also interacted with purine nucleotides in bacterial
350 PPATs [35-37] (Figs. 7G and S10F), partially explaining the competitive inhibition of the
351 enzyme by purine nucleotides. We introduced mutations at these aspartic acids (D373A
352 and D374A, referred to as Ade4-DA) and investigated whether the interaction with PRPP
353 affected the assembly of Ade4 condensates. Ade4-DA-mNG was virtually incapable of
354 forming punctate structures (Fig. 7H), demonstrating that the interaction with PRPP was
355 essential for the assembly of Ade4 condensates in cells.

356 Further purification of the mutant Ade4 protein allowed us to examine its *in vitro*
357 biochemical properties (Fig. S10G). Ade4-DA-mNG condensated into particles under
358 10% PEG conditions, similar to wild-type Ade4-mNG (Fig. S10H), indicating that the
359 mutation did not impair the self-assembly of Ade4 under crowding conditions. We found
360 that PRPP only negligibly promoted the assembly of Ade4-DA-mNG condensates (Fig.
361 7I), suggesting that the binding of PRPP at the catalytic site was responsible for
362 facilitating the condensation of Ade4 molecules. In contrast, the DA mutant remained
363 sensitive to AMP; AMP inhibited the assembly of Ade4-DA-mNG condensates, albeit
364 less effectively than that of Ade4-mNG condensates (Fig. 7J). Consistently, PRPP was
365 unable to counteract the inhibitory effects of AMP on the condensation of Ade4-DA, even
366 at concentrations higher than 500 μM (Figs. 7K and S10I-J). Therefore, while the
367 interaction of purine nucleotides at the PRPP binding motif partially contributed to the
368 inhibition of Ade4 condensation, purine nucleotides also appeared to suppress Ade4

369 condensation through additional binding sites (Fig. 7G).
370
371 MD calculations predict the possible condensation-dependent activation of PPAT
372 by enabling intermolecular substrate channeling
373 The induction of Ade4 condensate formation by the substrate PRPP prompted us to
374 propose that the condensation of Ade4 promotes its enzymatic activity. In glutamine-
375 dependent PRA synthesis (Gln-PRA activity, Fig. 8A), NH_3 is initially released from
376 glutamine at the GATase site and must then be transferred to PRPP at the PRTase site. A
377 structural analysis of *E. coli* PPAT suggested that PRPP binding creates a transient
378 hydrophobic channel linking the GATase and PRTase sites [34], thereby facilitating the
379 efficient intramolecular transfer of NH_3 between these catalytic sites (Figs. 8B-C and
380 S11A). However, this intramolecular substrate channeling may be independent of the
381 condensation state of the enzyme. In addition to glutamine-derived NH_3, PPAT also
382 directly utilize ambient NH_3 as a nitrogen donor to produce PRA, referred to as NH_3-
383 dependent PRA synthesis (NH_3-PRA activity, Figs. 8A and S11B) [6]. Based on a
384 condensation-dependent activation mechanism, we hypothesized that the Ade4
385 condensate may enable the intermolecular transfer of NH_3 between molecules (Fig. 8C,
386 right).
387 To test this hypothesis, we investigated the behavior of NH_3 on the PPAT molecule
388 by conducting MD simulations using the crystal structure of *E. coli* PPAT in its active
389 form [34]. MD simulations for the holo state of PPAT, which included glutamate, NH_3, PRPP,
390 and Mg^{2+}, showed that NH_3 mostly remained at the initial or adjacent positions during
391 ten trials and did not reach the catalytic site, despite the presence of the hydrophobic
392 channel (Fig. 8D). This result suggests a low frequency of intramolecular channeling
393 relative to our simulation time. In contrast, in the semi-holo state containing only
394 glutamate and NH_3, NH_3 escaped through the hydrophobic channel once in ten trials.
395 Unexpectedly, NH_3 was instead released from the molecule through a transient channel
396 directed towards Arg333 in four out of ten trials (Fig. 8E-F and Movie S8). This Arg333
397 is conserved in yeast Ade4 and is referred to as the front channel. Prior to the release of
398 NH_3, we noted that the hydrophobic side chain of Phe260 flipped from its initial structure.
399 Furthermore, Arg333 functioned as a gate for NH_3 by forming hydrogen bonds with the
400 backbone oxygen of Tyr259, Phe260, His26, and the phosphate group of PRPP (Fig. 8G).
401 Notably, the absence of PRPP increased structural fluctuations in the Arg gate in the semi-
402 holo state, thereby increasing the likelihood of gate opening.
403 Additional simulations on the Arg333Ala mutant under holo conditions confirmed
404 the critical role of this Arg gate. The flipping of Phe260 and subsequent release of NH_3

405 were observed in six out of ten trials on the Arg333Ala mutant, despite the presence of
406 PRPP at the catalytic site (Fig. 8H). This increased gate-opening frequency in the mutant
407 suggests that the normally closed Arg gate, coupled with PRPP, suppresses the flipping
408 of the Phe260 side chain and the release of NH_3. Since the PRTase catalytic site utilize
409 ambient NH_3 as a nitrogen donor [6], the release of PRA may simultaneously facilitate the
410 release of internal glutamine-derived NH_3 through the front channel (Fig. 8I and S11C).
411 Collectively, these simulation results support PPAT condensation facilitating the
412 intermolecular transfer of leaked NH_3 between closely located molecules, leading to the
413 efficient utilization of glutamine-derived NH_3 (Figs. 8C, right panel and S11D).
414

415 Formation of Ade4 condensates is important for efficient *de novo* purine synthesis
416 during cell growth

417 Authentic Gln-PRA activity and NH_3-PRA activity (Fig. 8A) have both been
418 implicated in the *de novo* biosynthesis of purine nucleotides *in vivo* [38 39]. Since NH_3-PRA
419 activity depends on the concentration of NH_4^+ in medium, a fraction of which is present
420 as NH_3 [6], Ade4 condensates may be critical for Gln-PRA activity under low ammonium
421 conditions. To examine this possibility, we compared the growth of cells expressing wild-
422 type Ade4 with those expressing the Ade4ΔIDR mutant, which is unable to form
423 condensates *in vivo*. On solid medium without adenine, the growth of the 3×HA-tagged
424 Ade4ΔIDR cells was markedly slower than that of wild-type Ade4 cells (Fig. 9A). The
425 protein level of Ade4ΔIDR grown in adenine-free medium was similar to that of wild-
426 type Ade4 (Fig. 9B). Supplementation with adenine restored the growth of the
427 *ADE4ΔIDR* mutant to wild-type rates, indicating that the slow growth of the mutant was
428 due to reduced enzyme activity rather than dominant-negative inhibition by the mutant
429 protein. Notably, the growth of the *ADE4ΔIDR* mutant significantly decreased with
430 reductions in the concentration of ammonium ions from ammonium sulfate (AS) in the
431 medium (Fig. 9A). We further quantified cell growth by measuring growth curves in
432 liquid medium. The *ADE4ΔIDR* mutant exhibited significantly slower growth,
433 particularly in the absence of ammonium ions, while the growth rate of the wild-type
434 strain remained almost independent of the ammonium ion concentration in the medium
435 (Fig. 9C-D). Collectively, these results suggest that the condensation of Ade4 into
436 particles is critical for *de novo* purine synthesis, particularly under low ammonium
437 conditions, where Gln-PRA activity plays a pivotal role.
438

Discussion

We demonstrated that the budding yeast PPAT forms intracellular condensates through TORC1-mediated macromolecular crowding and PRPP-dependent self-assembly to regulate *de novo* purine synthesis in response to extracellular purine bases (Fig. 10). MD simulations revealed a previously unidentified pathway by which an intermediate NH_3 derived from glutamine leaks from the PPAT molecule (Figs. 8I and S11C). We propose that Ade4 condensation enhances Gln-PRA activity by facilitating a domino-like chain reaction through intermolecular intermediate channeling. The condensation of PPAT, which has two catalytic domains, is considered to be equivalent to the co-clustering of two distinct enzymes, GATase and PRTase, in a confined space. Although NH_3 is expected to diffuse rapidly throughout the cytoplasm [40], within Ade4 condensates—where the enzyme concentration is high—another enzyme may capture NH_3 and effectively process it by the PRTase domain (Figs. 8C, right panel and S11D). This form of enzyme activation by intermolecular NH_3 channeling corresponds to clustering-mediated metabolic channeling theoretically predicted by Castellana et al. [41]. The present study is the first demonstration that a native enzyme may be activated by this type of metabolic channeling in eukaryotic cells.

Recent studies revealed that many metabolic enzymes form intracellular condensates by phase separation, allowing cellular metabolism to adapt to variable growth conditions [9]. These condensates serve as temporary stores for inactive enzymes, helping cells survive adverse environmental conditions[9]. In some cases, filament formation by the enzyme enhances catalytic activity[42, 43]. Our results add another example where the condensation of a metabolic enzyme boosts catalytic activation through intermolecular substrate channeling. Notably, Ade4 condensates are unique among the cellular condensates reported to date due to their dynamic nature; they assemble and disassemble quickly and reversibly in response to environmental purine bases and exhibit high motility.

Ade4 (PPAT) condensates resemble enzyme clusters known as purinosomes, which form reversibly in HeLa cells under purine deprivation [13]. Purinosomes enhance the channeling of metabolic intermediates in the *de novo* pathway near mitochondria, thereby increasing pathway flux [14]. However, these two structures differ in several respects. Purinosomes contain all six enzymes involved in *de novo* purine synthesis with formylglycinamidine ribonucleotide synthase as the core, whereas cellular clusters of PPAT are smaller and only some colocalize with purinosomes[44]. Furthermore, purinosomes are static, assembling and disassembling in approximately 1.5 and 1 h, respectively, and are non-motile[13]. Therefore, we hypothesize that PPAT condensates are

475 structurally distinct from purinosomes and may coexist inside or outside of them. Since
476 PPAT is the rate-limiting enzyme in *de novo* purine synthesis, its condensates may provide
477 a rapid and flexible response to fluctuations in environmental purine base levels, whereas
478 purinosomes may represent a more constant adaptation to purine scarcity.
479 We also found that purified Ade4 self-assembled into fine particles under molecular
480 crowding conditions. *In vitro* phase separation assays further demonstrated that Ade4
481 condensation involved both IDR-independent self-assembly and IDR-dependent
482 condensation. In addition to the C-terminal IDR, the Ade4 protein has a short putative
483 IDR at the N terminus. Consistently, plant and insect PPATs have an IDR at the N
484 terminus, but not at the C terminus, suggesting that both ends of the protein may
485 contribute to condensate formation by phase separation. Therefore, multiple IDRs may
486 be involved in complete condensate formation. Nevertheless, it is intriguing to speculate
487 that C-terminal IDR-independent self-assembly is essential for subsequent IDR-
488 dependent condensation, where phase separation is required for stable condensation into
489 particles (see Fig. 10, right panel).
490
491 The enzymatic activity of PPAT is considered to be regulated in a feedback manner
492 by millimolar levels of AMP and GMP [45]. However, intracellular purine mononucleotide
493 concentrations are generally maintained in the micromolar range, from tens to hundreds,
494 and are not markedly affected by extracellular purine bases (Fig. 4D and previous
495 studies[46-48]). Therefore, this feedback regulation appears to be physiologically irrelevant,
496 at least in response to environmental purine bases. In contrast, the present results indicate
497 that purine nucleotides inhibit the IDR-independent self-assembly of Ade4, while PRPP
498 promotes condensate formation *in vitro*. We speculate that these two regulators control
499 the assembly of Ade4 condensates, thereby affecting PPAT enzyme activity *in vivo*. Since
500 ADP and ATP, similar to AMP, suppressed the assembly of Ade4 condensates, GDP and
501 GTP may also exert similar inhibitory effects to those of GMP. Therefore, the
502 concentrations of all purine nucleotides may be physiologically relevant and sufficient to
503 exert inhibitory effects on Ade4 condensate formation in cells.
504 The intracellular concentrations of purine nucleotides were previously shown to
505 slightly increase in the presence of environmental purine bases [46-48], while that of PRPP
506 decreased to approximately 10 μM. At this level, PRPP is unable to interact with Ade4 in
507 order to promote its assembly, and, thus, purine nucleotides may predominantly interact
508 with Ade4 and prevent condensate formation. In the absence of purine bases, PRPP levels
509 may increase up to several tens of micromolar, thereby promoting the condensation of
510 Ade4. Since PRPP-docked Ade4 is prone to condensation, the local concentration of

511 PRPP within condensates is expected to markedly increase. Consistent with this notion,
512 the K_m of PPAT for PRPP in yeast was previously reported to be 110 μM[49], which is 3.7-
513 fold higher than the intracellular concentration of PRPP even in the absence of adenine.
514 Similarly, in mammals, intracellular PRPP concentrations range between 5 and 30 μM[50],
515 while the enzyme's K_m for PRPP is 480 μM[51]. The enrichment of PRPP within Ade4
516 condensates provides an example of the spatial control of substrate concentrations by
517 biomolecular condensates[52].
518 Consistent with the present results, the binding of PRPP to the specific binding motif
519 at the catalytic site of *E. coli* PPAT has been reported to induce a structural change in the
520 enzyme [34, 53], which may contribute to the enhanced clustering of the enzyme under
521 molecular crowding conditions. AMP also interacts with the PRPP binding motif;
522 however, in contrast to PRPP, it inhibits self-assembly. Therefore, competitive binding
523 to the motif explains the mechanism by which PRPP counteracts the effects of purine
524 nucleotides. However, since the Ade4-DA mutant remains sensitive to inhibition by AMP,
525 further structural analyses are required to elucidate the assembly mechanisms and effects
526 of purine nucleotides.
527 It is important to note that the addition of purine bases to culture media was found to
528 reduce the concentration of PRPP in both bacterial cells [50] and mammalian cells [54],
529 suggesting a conserved mechanism across species. The most likely explanation for this is
530 the consumption of PRPP, coupled with the conversion of incorporated purine bases by
531 hypoxanthine-guanine phosphoribosyltransferase (HGPRT, known as Hpt1 in budding
532 yeast). HGPRT utilizes PRPP as a substrate more efficiently than PPAT, as evidenced by
533 its markedly lower K_m for PRPP[55]. Consistently, HGPRT-negative lymphoblasts from
534 Lesch-Nyhan syndrome patients showed 4- to 8-fold higher intracellular PRPP levels than
535 those from normal individuals[56], which supports this notion and is consistent with the
536 phenotype of *hpt1*Δ cells observed in the present study.
537
538 We found that ribosome biogenesis downstream of TORC1 signaling was required
539 for Ade4 condensate formation. These results align with the theory that TORC1 regulates
540 macromolecular crowding of the cytoplasm through ribosome synthesis, which, in turn,
541 controls biomolecular condensation by phase separation [20]. The present study is the first
542 experimental demonstration of a metabolic enzyme assembling into condensates via the
543 TORC1-regulated phase transition of the cytoplasm (see Fig. 10, left panel). Since
544 TORC1 and PPAT IDRs are both conserved across many species, the condensation of
545 PPAT by TORC1 may represent a common feature in eukaryotic cells.
546 The involvement of TORC1 is another crucial aspect of Ade4 condensates. TORC1

547 is activated by sensing nutrients, such as amino acids and glucose [57]. Therefore, the
548 requirement of TORC1 activity for PPAT condensation ensures that the *de novo* synthesis
549 of purines is maximized under conditions that are favorable for cell growth. In mammals,
550 TORC1 transcriptionally up-regulates the enzymes involved in the mitochondrial
551 tetrahydrofolate cycle, thereby increasing *de novo* purine synthesis [58]. Correlating the
552 metabolic flux of purine synthesis with the nutritional status via TORC1 activity appears
553 to be a conserved and multi-layered regulatory mechanism for cell proliferation.
554 Disorders in the regulation of purine metabolism are associated with various diseases,
555 such as cancer, hyperuricemia (gout), and immunological defects [59, 60]. A more detailed
556 examination of purine metabolism will provide insights into the molecular mechanisms
557 underlying these diseases. Importantly, a recent study implicated the up-regulation of
558 PPAT in the malignant progression of many cancer types [61]. Therefore, elucidating the
559 regulatory mechanism of PPAT activity will not only enhance our understanding of purine
560 metabolism in a biological context, but also contribute to advances in basic and
561 therapeutic research on cancer.
562

563 **Materials and Methods**

564 Yeast strains and plasmids

565 The yeast strains, plasmids, and primers used in the present study are listed in
566 Supplementary Tables S1, S2, and S3, respectively. These strains were constructed by a
567 PCR-based method [62] and genetic crosses. The yeast knockout strain collection was
568 originally purchased from GE Healthcare (cat. # YSC1053).

569

570 Regarding the construction of plasmids used for the C-terminal tagging of monomeric
571 GFP or mKate2, DNA fragments encoding the corresponding fluorescent proteins were
572 artificially synthesized (Eurofin Genomics, Ebersberg, Germany). These fragments were
573 replaced with GFP of pYM25[62] using *Sal*I/*Bgl*II sites to yield MTP3114 and MTP3131,
574 respectively. The plasmid used for the C-terminal tagging of mNG-Strep tag II
575 (MTP3139) was constructed in the same manner: a DNA fragment encoding single mNG
576 fused with the Strep II tag (WSHPQFEK) by a spacer sequence (ELYKGSA) was
577 synthesized and then replaced with the GFP of pYM25.

578

579 Media and cell culture

580 Synthetic medium optimized for the growth of the BY strain was prepared as described
581 by Hanscho et al. [63]. Growth assays in solid and liquid media used optimized synthetic
582 media lacking glutamate, phenylalanine, serine, and threonine. Yeast nitrogen base
583 without amino acids, but with AS (cat. # Q30009) was purchased from Invitrogen. Yeast
584 nitrogen base without amino acids and AS (cat. # CYN0501) was obtained from
585 FORMEDIUM. Synthetic medium without ammonium sulphate was supplemented with
586 8 mM proline as an alternative nitrogen source. Rich medium was standard YPD medium
587 composed of 1% (w/v) yeast extract (BD, cat. # 212750), 2% (w/v) bacto-peptone (BD,
588 cat. # 211677), and 2% (w/v) D-glucose. Glucose (cat. # 049-31165), adenine sulfate (cat.
589 # 018-10613), hypoxanthine (cat. # 086-03403), 1, 6-hexanediol (cat. # 087-00432), and
590 digitonin (cat. # 043-2137) were purchased from FUJIFILM Wako. Cells were grown to
591 the mid-log phase at 30°C before imaging unless otherwise noted. To replace medium
592 containing adenine with medium lacking adenine, cells were collected in a microtube by
593 brief centrifugation and suspended in medium lacking adenine. This washing procedure
594 was repeated at least twice. Rapamycin was purchased from LC Laboratories (cat. # R-
595 5000).

596

597 Microscopy

598 Cells expressing a GFP-fusion protein were concentrated by centrifugation and

599 sandwiched between a slide and coverslip (No. 1.5 thickness, Matsunami, Osaka, Japan).
600 Immobilized cells were imaged using an inverted fluorescent microscope (Eclipse Ti2-E,
601 Nikon, Tokyo, Japan) equipped with a CFI Plan Apoλ 100× Oil DIC/NA1.45 objective
602 lens and CMOS image sensor (DS-Qi2, Nikon). The fluorescent signal was collected
603 from stacks of 11 *z*-sections spaced by 0.5 μm, and the maximum projections of optical
604 sections were shown unless otherwise noted. A CFI Plan Apoλ 60× Oil Ph3 DM/NA1.40
605 or CFI Plan Apoλ 100× Oil Ph3 DM/NA1.45 objective lens was used for phase contrast
606 imaging. Images of cells were acquired from several fields of view for each experimental
607 condition. All digital images were processed with the Fiji image platform[64].
608

609 Quantitative analysis of intracellular fluorescent condensation

610 Intracellular fluorescent condensation (*i.e.*, Ade4-GFP foci or Ade4-mNG particles) was
611 automatically detected and analyzed by running Fiji macros
612 (https://github.com/masaktakaine/FP-foci-quantification and
613 https://github.com/masaktakaine/FP-granules-quantification). Briefly, these macros
614 extract cell outlines from phase-contrast images and detect fluorescent condensation
615 inside the cell boundary using the *FindMaxima* function of Fiji software.
616
617 To monitor temporal changes in the number of intracellular Ade4-mNG particles by time-
618 lapse imaging, the number of maxima of green fluorescence intensity in the field was
619 counted in each time frame and divided by the total cell number by running a Fiji macro
620 (https://github.com/masaktakaine/Counting-FP-granules-in-time-lapse).
621 In cases in which phase-contrast images were unavailable, we manually examined
622 condensation.
623

624 Spot growth assay

625 Cells were grown to the mid-log phase at 30°C in synthetic medium, and cell density
626 (cells/ml) was measured by an automated cell counter (TC20, Bio-Rad). The culture was
627 diluted by medium lacking nitrogen and carbon sources to a density of 1×10^6 cells/ml,
628 serially diluted 5-fold, and spotted on plates. Plates were incubated at 30°C for 2-3 days
629 and then imaged by an image scanner (GT-X830, EPSON).
630

631 Measurement of growth curves in liquid cultures

632 Cell growth in liquid media was monitored in a 96-well flat-bottomed plate using a
633 microplate reader (iMark, Bio-Rad). Cells were grown to the mid-log phase and then

634 diluted to OD_{600} = 0.1. Each well was filled with 300 µl of the cell dilution and OD_{595}
635 was measured at 30°C every 10 min.
636
637 Immunoblot analysis
638 A denatured whole-cell extract was prepared according to the method reported by von der
639 Haar (2007) [65]. Briefly, mid-log cells were harvested from 2–3 ml of the culture by
640 centrifugation. The cell pellet was resuspended in a small volume (<100 µl) of lysis buffer
641 (0.1 M NaOH, 50 mM EDTA, 2% (w/v) SDS, and 2% (v/v) β-mercaptoethanol) and then
642 incubated at 90°C for 10 min. The sample was neutralized by the addition of a one-tenth
643 volume of 1 M acetic acid, incubated at 90°C for 10 min, and mixed with a one-third
644 volume of 4×Laemmli protein sample buffer (cat. # 1610747, Bio-Rad). Following
645 centrifugation at 20,000×*g* at 4°C for 10 min, the upper 90% of the supernatant was
646 collected as the clarified whole-cell extract and stored at -30°C until used. Proteins were
647 resolved by SDS-PAGE using a pre-cast gel containing 10% (w/v) acrylamide
648 (SuperSep™ Ace, cat. # 195-14951, FUJIFILM Wako) and then transferred onto a PVDF
649 membrane (Immobilon-P, Millipore) using a protein transfer system (Trans-Blot Turbo
650 Transfer System, Bio-Rad). HA-tagged Ade4 proteins were detected using an anti-HA
651 antibody (mouse monoclonal (12CA5), cat. # GTX16918, Funakoshi) at a 1:1000 dilution.
652 GFP-tagged proteins were detected using an anti-GFP antibody (mouse monoclonal
653 (1E10H7), cat. #66002-1-Ig, ProteinTech) at a 1:1000 dilution. GAPDH was detected
654 using an anti-GAPDH antibody (mouse monoclonal (1E6D9), cat. # 60004-1-Ig,
655 ProteinTech) at a 1:1000 dilution. PGK1 was detected using an anti-PGK1 antibody
656 (mouse monoclonal (22C5D8), cat. # ab113687, Abcam) at a 1:1000 dilution. An HRP-
657 conjugated secondary antibody (from sheep, cat. #NA931V, GE Healthcare) was probed
658 at a 1:10000 dilution. Immunoreactive bands were luminescent in a chemiluminescent
659 substrate (Western BLoT Quant HRP substrate, cat. # T7102A, TaKaRa) and imaged
660 using an image analyzer (LAS4000, GE Healthcare).
661
662 Protein purification from yeast cells
663 Ade4-mNG, Ade4ΔIDR-mNG, and mNG were C-terminally tagged with a single Strep-
664 tag II, expressed in budding yeast cells, and purified as follows. Yeast cells expressing
665 the tagged protein were grown in liquid YPD medium supplemented with 0.02 mg/ml
666 adenine sulfate at 30°C for at least 20 h. The pre-culture was diluted by 100- to 1000-fold
667 in 100 ml of fresh YPD plus adenine medium, and cells were further grown at 30°C to
668 4×10^7 cells/ml. Cells were harvested by centrifugation at 2,000×*g* and washed twice with
669 1 ml of extraction buffer (EB) (0.15 M NaCl, 1 mM EDTA, 1 mM dithiothreitol, and 40

670 mM Tris-HCl, pH 7.5) supplemented with 1 mM PMSF and cOmplete protease inhibitor
671 cocktail (EDTA-free) (Roche, cat. # 11836170001). One gram of glass beads with a
672 diameter of 0.5 mm (YASUI KIKAI, cat. # YGBLA05) was mixed with the cell
673 suspension, and cells were disrupted by vigorous shaking using a beads beater (YASUI
674 KIKAI, MB901). The crude cell extract was collected by brief centrifugation, and glass
675 beads were washed with a small volume of EB (<0.5 ml). The crude extract and washes
676 were combined and clarified by centrifugation twice at 20,000×*g* at 4°C for 10 min. To
677 block endogenous biotin, the cleared lysate was supplemented with 0.2 mg/ml neutralized
678 avidin (FUJIFILM Wako, cat. # 015-24231), incubated on ice for 30 min, and clarified
679 by centrifugation at 20,000×*g* at 4°C for 10 min. The supernatant was loaded onto a
680 handmade open column packed with 0.5 ml of Strep-Tactin Sepharose (IBA GmbH, cat.
681 # 2-1201-002). After washing with 10 column volumes of EB, bound proteins were eluted
682 with 6 column volumes of EB plus 2.5 mM D-desthiobiotin (IBA GmbH, cat. # 2-1000-
683 025). The protein amounts and compositions of elution fractions were analyzed by SDS-
684 10% PAGE and stained with FastGene Q-stain (Nippon Genetics, cat. # NE-FG-QS1).
685 Peak fractions were pooled and concentrated using an Amicon Ultra-0.5 centrifugal filter
686 device with a molecular weight cut-off of 30 or 10 kDa (Merck, cat. # UFC503024 or
687 UFC501008). D-desthiobiotin in the peak fraction was diluted more than 100-fold by a
688 repeating dilution with EB and the centrifugal concentration. The concentration of the
689 purified protein was assessed by densitometry using bovine serum albumin (TaKaRa, cat.
690 # T9310A) as a standard following SDS-PAGE and staining with the Q-stain. Purified
691 Ade4-mNG and Ade4ΔIDR-mNG were supplemented with 10 mM DTT and stored on
692 ice.
693
694 *In vitro* condensation assay
695 The purified protein was diluted to the indicated concentration in assay buffer (EB plus 5
696 mM $MgCl_2$) and supplemented with 0–15% (w/v) PEG 8000 (FUJIFILM Wako, cat. #
697 596-09755). In the experiments shown in Fig. S4C-E, samples were spiked with 10%
698 (w/v) PEG of the indicated molecular size. The mixture was immediately loaded into an
699 assay chamber composed of a glass slide and coverslip attached by double-sided tape.
700 Images were taken after a 2-min incubation. Fluorescent condensation was imaged using
701 the Nikon inverted fluorescent microscope (see above). Images of fluorescent
702 condensation were analyzed by running a Fiji macro
703 (https://github.com/masaktakaine/In-vitro-condensates-quantification). Briefly, the
704 macro automatically detects fluorescent condensation and quantifies its area and
705 fluorescence intensity.

706

707 Quenching of yeast cells for a metabolomics analysis

708 The quenching of yeast cells before metabolite extraction followed the method reported
709 by Kim et al. [66] with slight modifications. Wild-type BY4741 cells were grown to
710 saturation in YPD medium, inoculated into synthetic medium with or without 0.02 mg/ml
711 adenine, and then grown at 30°C for more than 16 hours. The preculture was diluted 50–
712 60 times with 10 ml of fresh medium, and cells were grown to approximately 1.0×10^7
713 cells/ml at 30°C. After measuring cell density (cells/ml) with an automated cell counter
714 (TC20, Bio-Rad), 0.9 ml of the cell culture was quenched by a rapid injection into 4.5 ml
715 of pure methanol at −80°C. The suspension was centrifuged at 2,200×*g* at 4°C for 3 min,
716 and the cell pellet was stored at −80°C until extraction. In samples labeled "- ade" and
717 "+ade 24h", cells were cultured for more than 24 h (since the pre-culture) in medium
718 containing 0 or 0.02 mg/ml adenine, respectively. In samples labeled as "+ade 1h" and
719 "+ade 7h", adenine was added at a final concentration of 0.02 mg/ml 1 or 7 h before
720 quenching, respectively.

721

722 Metabolite extraction and widely targeted metabolomics profiling

723 A widely targeted metabolomic analysis was performed as previously described [67]. In
724 brief, each frozen sample in a 1.5-mL plastic tube was homogenized in 200 μL of 50%
725 methanol with glass beads using a microtube homogenizer (TAITEC Corp.) at 41.6 Hz
726 for 2 min. Homogenates were mixed with 400 μL of methanol, 100 μL of H_2O, and 200
727 μL of $CHCl_3$ and vortexed for 20 min. Samples were centrifuged at 20,000×*g* at 4°C for
728 15 min. The supernatant was mixed with 350 μL of H_2O, vortexed for 10 min, and
729 centrifuged at 20,000×*g* at 4°C for 15 min. The aqueous phase was collected, dried in a
730 vacuum concentrator, and re-dissolved in 2 mM ammonium bicarbonate (pH 8.0).
731 Chromatographic separations were performed using an Acquity UPLC H-Class System
732 (Waters) under reverse-phase conditions with an ACQUITY UPLC HSS T3 column (100
733 × 2.1 mm, particle size of 1.8 μm, Waters) and under HILIC conditions using an
734 ACQUITY UPLC BEH Amide column (100 × 2.1 mm, particle size of 1.7 μm, Waters).
735 Ionized compounds were detected using a Xevo TQD triple quadrupole mass
736 spectrometer coupled to an electrospray ionization source (Waters). The peak areas of
737 target metabolites were analyzed using MassLynx 4.1 software (Waters). Metabolite
738 signals were normalized to total ion signals of the corresponding sample. To estimate
739 absolute PRPP concentrations, the amount of PRPP in the sample was quantified by
740 comparisons with standard curves obtained for pure PRPP. Intracellular concentrations
741 were then calculated using the previously reported haploid yeast cell volume (42 fL)[68].

742

743 ## MD simulation

744 The crystal structure of *E. coli* PPAT (PDB ID: 1ECC) was obtained from the Protein
745 Data Bank and used for all MD simulations [34]. All water molecules and ions were
746 removed before simulations. To build the parameters of ligands (NH_3, PRPP, and glutamic
747 acid), their restrained electrostatic potential charges were calculated based on gas-phase
748 HF/6-31(d) quantum mechanics calculations using Gaussian 16. A set of parameters were
749 generated with a general AMBER force field using the antechamber from AMBER tools
750 [69].

751

752 The Amber ff14SB force field was employed for all MD simulations [70]. Missing hydrogen
753 atoms were added by LEaP from AMBER tools. Proteins were solvated with the TIP3P
754 water box [71]. The system was neutralized by replacing water with Na^+ or Cl^- ions. The
755 particle-mesh Ewald method was employed for the Coulomb interaction [72]. Amber-
756 formatted input files were converted for GROMACS using acpype [73]. All MD simulations
757 were performed using GROMACS 2019.6 [74]. Before the production run, three-step
758 equilibrations were performed for each system. Energy minimization was performed until
759 10,000 steps. This was followed by 100-ps *NVT* equilibration with the V-rescale
760 thermostat [75] at 300 K under 1 atm. A 100-ps *NPT* equilibration was then conducted with
761 Berendsen coupling [76] at 300 K under 1 atm. A run was performed under the *NPT*
762 condition. The time step of each simulation was 2 fs with the SHAKE [77] and SETTLE [78]
763 algorithms, and a snapshot was recorded every 100 ps during the production run. To
764 examine the results of MD simulations, a Python library MDanalysis was used [79].

765

766 ## Data analysis

767 Numerical data were analyzed and plotted using R studio software (R ver. 4.3.1) [80]. Box
768 plots show the 75th and 25th percentiles of data (interquartile range) as the upper and
769 lower edges of the box, respectively, the median as the medial line in the box, and the
770 1.5×interquartile range as whiskers. The significance of differences between sets of data
771 was indicated by asterisk(s) or *p*-values. The following abbreviations were used unless
772 otherwise noted: *, $p < 0.05$; **, $p < 0.01$; ***, $p < 0.001$; NS, not significant ($p > 0.05$).
773 Sparse PLS-DA was performed using the *splsda* function in the mixOmics R package[81].
774 A one-way ANOVA and subsequent adjustments of *p*-values by the Benjamini-Hochberg
775 method to control the false discovery rate (FDR) were performed using Metaboanalyst

6.0 (https://www.metaboanalyst.ca/MetaboAnalyst/home.xhtml). The top 25 metabolites whose changes strongly correlated with those in the intracellular concentration of adenine were identified using the pattern hunter analysis of Metaboanalyst. All measurements were repeated at least twice to confirm reproducibility.

Acknowledgments

The authors thank the IMCR-JURSC in Gunma University for sharing research equipment. This work was supported by research grants from the Gout and Uric Acid Foundation of Japan and by JSPS KAKENHI Grant Number JP22K06216 to M.T. This work was also supported by the joint research program of the Institute for Molecular and Cellular Regulation, Gunma University, Japan. This study used the computational resources of Cygnus provided by the Multidisciplinary Cooperative Research Program at the Center for Computational Sciences (Project Code: MOLBIO), University of Tsukuba.

Author Contributions

MT conceived and supervised the study. MT and RM designed the experiments. MT, YY, and TN performed the experiments. RM performed MD simulations. MT, RM, YY, and TN analyzed the data. MT wrote the manuscript draft with input from RM. All authors discussed and reviewed the manuscript.

Declaration of Interests

The authors declare no competing interests.

References

1. Yamaoka, T. *et al.* Amidophosphoribosyltransferase Limits the Rate of Cell Growth-linked de Novo Purine Biosynthesis in the Presence of Constant Capacity of Salvage Purine Biosynthesis. *Journal of Biological Chemistry* **272**, 17719-17725 (1997).
2. Gots, J.S. Purine Metabolism in Bacteria. *Journal of Biological Chemistry* **228**, 57-66 (1957).
3. Pedley, A.M. & Benkovic, S.J. A New View into the Regulation of Purine Metabolism: The Purinosome. *Trends Biochem Sci* **42**, 141-154 (2017).
4. Yamaoka, T. *et al.* Feedback inhibition of amidophosphoribosyltransferase regulates the rate of cell growth via purine nucleotide, DNA, and protein syntheses. *J Biol Chem* **276**, 21285-21291 (2001).
5. Meyer, E. & Switzer, R.L. Regulation of Bacillus subtilis glutamine phosphoribosylpyrophosphate amidotransferase activity by end products. *J Biol Chem* **254**, 5397-5402 (1979).
6. Messenger, L.J. & Zalkin, H. Glutamine phosphoribosylpyrophosphate amidotransferase from Escherichia coli. Purification and properties. *J Biol Chem* **254**, 3382-3392 (1979).
7. Jimenez, A., Santos, M.A., Pompejus, M. & Revuelta, J.L. Metabolic engineering of the purine pathway for riboflavin production in Ashbya gossypii. *Appl Environ Microbiol* **71**, 5743-5751 (2005).
8. Park, J.O. *et al.* Metabolite concentrations, fluxes and free energies imply efficient enzyme usage. *Nat Chem Biol* **12**, 482-489 (2016).
9. Prouteau, M. & Loewith, R. Regulation of Cellular Metabolism through Phase Separation of Enzymes. *Biomolecules* **8** (2018).
10. Cereghetti, G. *et al.* Reversible amyloids of pyruvate kinase couple cell metabolism and stress granule disassembly. *Nat Cell Biol* **23**, 1085-1094 (2021).
11. Saad, S. *et al.* Reversible protein aggregation is a protective mechanism to ensure cell cycle restart after stress. *Nature Cell Biology* **19**, 1202 (2017).
12. Narayanaswamy, R. *et al.* Widespread reorganization of metabolic enzymes into reversible assemblies upon nutrient starvation. *Proc Natl Acad Sci U S A* **106**, 10147-10152 (2009).
13. An, S., Kumar, R., Sheets, E.D. & Benkovic, S.J. Reversible compartmentalization of de novo purine biosynthetic complexes in living cells. *Science* **320**, 103-106 (2008).
14. Pareek, V., Tian, H., Winograd, N. & Benkovic, S.J. Metabolomics and mass spectrometry imaging reveal channeled de novo purine synthesis in cells. *Science* **368**, 283 (2020).
15. Noree, C. *et al.* A quantitative screen for metabolic enzyme structures reveals patterns of assembly across the yeast metabolic network. *Mol Biol Cell* **30**, 2721-2736 (2019).
16. Zacharias, D.A., Violin, J.D., Newton, A.C. & Tsien, R.Y. Partitioning of lipid-modified monomeric GFPs into membrane microdomains of live cells. *Science* **296**, 913-916 (2002).
17. Kroschwald, S., Maharana, S. & Simon, A. Hexanediol: a chemical probe to investigate the

835 material properties of membrane-less compartments. *Matters* (2017).
836 18. Uversky, V.N. Intrinsically disordered proteins in overcrowded milieu: Membrane-less organelles,
837 phase separation, and intrinsic disorder. *Curr Opin Struct Biol* **44**, 18-30 (2017).
838 19. Jones, D.T. & Cozzetto, D. DISOPRED3: precise disordered region predictions with annotated
839 protein-binding activity. *Bioinformatics* **31**, 857-863 (2015).
840 20. Delarue, M. *et al.* mTORC1 Controls Phase Separation and the Biophysical Properties of the
841 Cytoplasm by Tuning Crowding. *Cell* **174**, 338-349.e320 (2018).
842 21. Heitman, J., Movva, N.R. & Hall, M.N. Targets for cell cycle arrest by the immunosuppressant
843 rapamycin in yeast. *Science* **253**, 905-909 (1991).
844 22. Jorgensen, P. *et al.* A dynamic transcriptional network communicates growth potential to ribosome
845 synthesis and critical cell size. *Genes Dev* **18**, 2491-2505 (2004).
846 23. Beck, T. & Hall, M.N. The TOR signalling pathway controls nuclear localization of nutrient-
847 regulated transcription factors. *Nature* **402**, 689-692 (1999).
848 24. Lempiainen, H. *et al.* Sfp1 interaction with TORC1 and Mrs6 reveals feedback regulation on TOR
849 signaling. *Mol Cell* **33**, 704-716 (2009).
850 25. Fingerman, I., Nagaraj, V., Norris, D. & Vershon, A.K. Sfp1 plays a key role in yeast ribosome
851 biogenesis. *Eukaryot Cell* **2**, 1061-1068 (2003).
852 26. Pertschy, B. *et al.* Diazaborine Treatment of Yeast Cells Inhibits Maturation of the 60S Ribosomal
853 Subunit. *Molecular and Cellular Biology* **24**, 6476-6487 (2004).
854 27. Rebora, K., Desmoucelles, C., Borne, F., Pinson, B. & Daignan-Fornier, B. Yeast AMP pathway
855 genes respond to adenine through regulated synthesis of a metabolic intermediate. *Mol Cell Biol*
856 **21**, 7901-7912 (2001).
857 28. Valvezan, A.J. & Manning, B.D. Molecular logic of mTORC1 signalling as a metabolic rheostat.
858 *Nature Metabolism* **1**, 321-333 (2019).
859 29. Hoxhaj, G. *et al.* The mTORC1 Signaling Network Senses Changes in Cellular Purine Nucleotide
860 Levels. *Cell Rep* **21**, 1331-1346 (2017).
861 30. Emmanuel, N. *et al.* Purine Nucleotide Availability Regulates mTORC1 Activity through the Rheb
862 GTPase. *Cell Rep* **19**, 2665-2680 (2017).
863 31. Ferreira, T., Brethes, D., Pinson, B., Napias, C. & Chevallier, J. Functional analysis of mutated
864 purine-cytosine permease from Saccharomyces cerevisiae. A possible role of the hydrophilic
865 segment 371-377 in the active carrier conformation. *J Biol Chem* **272**, 9697-9702 (1997).
866 32. Jayaram, H.N. *et al.* Metabolites of alanosine, an antitumor antibiotic. *Biochem Pharmacol* **28**,
867 3551-3566 (1979).
868 33. Weng, M. & Zalkin, H. Mutations in the Bacillus subtilis purine repressor that perturb PRPP
869 effector function in vitro and in vivo. *Curr Microbiol* **41**, 56-59 (2000).
870 34. Krahn, J.M. *et al.* Coupled formation of an amidotransferase interdomain ammonia channel and a

871 phosphoribosyltransferase active site. *Biochemistry* **36**, 11061-11068 (1997).
872 35. Chen, S. *et al.* Mechanism of the synergistic end-product regulation of Bacillus subtilis glutamine
873 phosphoribosylpyrophosphate amidotransferase by nucleotides. *Biochemistry* **36**, 10718-10726
874 (1997).
875 36. Muchmore, C.R., Krahn, J.M., Kim, J.H., Zalkin, H. & Smith, J.L. Crystal structure of glutamine
876 phosphoribosylpyrophosphate amidotransferase from Escherichia coli. *Protein Sci* **7**, 39-51 (1998).
877 37. Smith, J.L. *et al.* Structure of the allosteric regulatory enzyme of purine biosynthesis. *Science* **264**,
878 1427-1433 (1994).
879 38. Mantsala, P. & Zalkin, H. Glutamine amidotransferase function. Replacement of the active-site
880 cysteine in glutamine phosphoribosylpyrophosphate amidotransferase by site-directed
881 mutagenesis. *J Biol Chem* **259**, 14230-14236 (1984).
882 39. Mei, B. & Zalkin, H. A Cysteine-Histidine-Aspartate Catalytic Triad Is Involved in Glutamine
883 Amide Transfer-Function in Purf-Type Glutamine Amidotransferases. *Journal of Biological*
884 *Chemistry* **264**, 16613-16619 (1989).
885 40. Antonenko, Y.N., Pohl, P. & Denisov, G.A. Permeation of ammonia across bilayer lipid
886 membranes studied by ammonium ion selective microelectrodes. *Biophysical Journal* **72**, 2187-
887 2195 (1997).
888 41. Castellana, M. *et al.* Enzyme clustering accelerates processing of intermediates through metabolic
889 channeling. *Nature Biotechnology* **32**, 1011-+ (2014).
890 42. Lynch, E.M. *et al.* Human CTP synthase filament structure reveals the active enzyme conformation.
891 *Nat Struct Mol Biol* **24**, 507-514 (2017).
892 43. Hunkeler, M. *et al.* Structural basis for regulation of human acetyl-CoA carboxylase. *Nature* **558**,
893 470-474 (2018).
894 44. Pedley, A.M. & Benkovic, S.J. Detecting Purinosome Metabolon Formation with Fluorescence
895 Microscopy. *Methods Mol Biol* **1764**, 279-289 (2018).
896 45. Rodwell, V.W., Bender, D., Botham, K.M., Kennelly, P.J. & Weil, P.A. *Harpers Illustrated*
897 *Biochemistry 30th Edition*. (McGraw Hill LLC, 2015).
898 46. Gauthier, S. *et al.* Co-regulation of yeast purine and phosphate pathways in response to adenylic
899 nucleotide variations. *Mol Microbiol* **68**, 1583-1594 (2008).
900 47. Pinson, B., Ceschin, J., Saint-Marc, C. & Daignan-Fornier, B. Dual control of NAD(+) synthesis
901 by purine metabolites in yeast. *Elife* **8**, e43808 (2019).
902 48. Saint-Marc, C. *et al.* Phenotypic consequences of purine nucleotide imbalance in Saccharomyces
903 cerevisiae. *Genetics* **183**, 529-538, 521SI-527SI (2009).
904 49. Satyanarayana, T. & Kaplan, J.G. Regulation of the purine pathway in bakers yeast: activity and
905 feedback inhibition of phosphoribosyl-pyrophosphate amidotransferase. *Arch Biochem Biophys*
906 **142**, 40-47 (1971).

50. Hove-Jensen, B. *et al.* Phosphoribosyl Diphosphate (PRPP): Biosynthesis, Enzymology, Utilization, and Metabolic Significance. *Microbiology and Molecular Biology Reviews* **81**, 10.1128/mmbr.00040-00016 (2016).
51. Holmes, E.W., McDonald, J.A., McCord, J.M., Wyngaarden, J.B. & Kelley, W.N. Human glutamine phosphoribosylpyrophosphate amidotransferase. Kinetic and regulatory properties. *J Biol Chem* **248**, 144-150 (1973).
52. Banani, S.F., Lee, H.O., Hyman, A.A. & Rosen, M.K. Biomolecular condensates: organizers of cellular biochemistry. *Nat Rev Mol Cell Biol* **18**, 285-298 (2017).
53. Chen, S., Burgner, J.W., Krahn, J.M., Smith, J.L. & Zalkin, H. Tryptophan fluorescence monitors multiple conformational changes required for glutamine phosphoribosylpyrophosphate amidotransferase interdomain signaling and catalysis. *Biochemistry* **38**, 11659-11669 (1999).
54. Yoshida, M. & Hoshi, A. Mechanism of inhibition of phosphoribosylation of 5-fluorouracil by purines. *Biochemical Pharmacology* **33**, 2863-2867 (1984).
55. Gutensohn, W. Inherited disorders of purine metabolism — Underlying molecular mechanisms. *Klinische Wochenschrift* **62**, 953-962 (1984).
56. Wood, A.W., Becker, M.A. & Seegmiller, J.E. Purine nucleotide synthesis in lymphoblasts cultured from normal subjects and a patient with Lesch-Nyhan syndrome. *Biochemical Genetics* **9**, 261-274 (1973).
57. Takahara, T., Amemiya, Y., Sugiyama, R., Maki, M. & Shibata, H. Amino acid-dependent control of mTORC1 signaling: a variety of regulatory modes. *Journal of Biomedical Science* **27**, 87 (2020).
58. Ben-Sahra, I., Hoxhaj, G., Ricoult, S.J.H., Asara, J.M. & Manning, B.D. mTORC1 induces purine synthesis through control of the mitochondrial tetrahydrofolate cycle. *Science* **351**, 728-733 (2016).
59. Daignan-Fornier, B. & Pinson, B. Yeast to Study Human Purine Metabolism Diseases. *Cells* **8** (2019).
60. Pareek, V., Pedley, A.M. & Benkovic, S.J. Human de novo purine biosynthesis. *Crit Rev Biochem Mol Biol*, 1-16 (2020).
61. Kodama, M. *et al.* A shift in glutamine nitrogen metabolism contributes to the malignant progression of cancer. *Nat Commun* **11**, 1320 (2020).
62. Janke, C. *et al.* A versatile toolbox for PCR-based tagging of yeast genes: new fluorescent proteins, more markers and promoter substitution cassettes. *Yeast* **21**, 947-962 (2004).
63. Hanscho, M. *et al.* Nutritional requirements of the BY series of Saccharomyces cerevisiae strains for optimum growth. *FEMS Yeast Res* **12**, 796-808 (2012).
64. Schindelin, J. *et al.* Fiji: an open-source platform for biological-image analysis. *Nat Methods* **9**, 676-682 (2012).
65. von der Haar, T. Optimized protein extraction for quantitative proteomics of yeasts. *PLoS One* **2**, e1078 (2007).

66. Kim, S. *et al.* Evaluation and Optimization of Metabolome Sample Preparation Methods for Saccharomyces cerevisiae. *Analytical Chemistry* **85**, 2169-2176 (2013).
67. Yamada, T. *et al.* The role of glycogen in development and adult fitness in Drosophila. *Development* **146** (2019).
68. Jorgensen, P., Nishikawa, J.L., Breitkreutz, B.J. & Tyers, M. Systematic identification of pathways that couple cell growth and division in yeast. *Science* **297**, 395-400 (2002).
69. D.A. Case, H.M.A., K. Belfon, I.Y. Ben-Shalom, J.T. Berryman, S.R. Brozell, D.S. Cerutti, T.E. Cheatham, III, G.A. Cisneros, V.W.D. Cruzeiro, T.A. Darden, R.E. Duke, G. Giambasu, M.K. Gilson, H. Gohlke, A.W. Goetz, R. Harris, S. Izadi, S.A. Izmailov, K. Kasavajhala, M.C. Kaymak, E. King, A. Kovalenko, T. Kurtzman, T.S. Lee, S. LeGrand, P. Li, C. Lin, J. Liu, T. Luchko, R. Luo, M. Machado, V. Man, M. Manathunga, K.M. Merz, Y. Miao, O. Mikhailovskii, G. Monard, H. Nguyen, K.A. O'Hearn, A. Onufriev, F. Pan, S. Pantano, R. Qi, A. Rahnamoun, D.R. Roe, A. Roitberg, C. Sagui, S. Schott-Verdugo, A. Shajan, J. Shen, C.L. Simmerling, N.R. Skrynnikov, J. Smith, J. Swails, R.C. Walker, J Wang, J. Wang, H. Wei, R.M. Wolf, X. Wu, Y. Xiong, Y. Xue, D.M. York, S. Zhao, and P.A. Kollman (University of California, San Francisco.; 2022).
70. Maier, J.A. *et al.* ff14SB: Improving the Accuracy of Protein Side Chain and Backbone Parameters from ff99SB. *J Chem Theory Comput* **11**, 3696-3713 (2015).
71. Kiss, P.T. & Baranyai, A. Sources of the deficiencies in the popular SPC/E and TIP3P models of water. *The Journal of Chemical Physics* **134**, 054106 (2011).
72. Pippig, M. & Mercuri, F. Efficient evaluation of Coulomb interactions in kinetic Monte Carlo simulations of charge transport. *The Journal of Chemical Physics* **152**, 164102 (2020).
73. Sousa da Silva, A.W. & Vranken, W.F. ACPYPE - AnteChamber PYthon Parser interfacE. *BMC Res Notes* **5**, 367 (2012).
74. M.J. Abraham, D.v.d.S., E. Lindahl, B. Hess, and the GROMACS development team (2019).
75. Bussi, G., Donadio, D. & Parrinello, M. Canonical sampling through velocity rescaling. *J Chem Phys* **126**, 014101 (2007).
76. Berendsen, H.J.C., Postma, J.P.M., van Gunsteren, W.F., DiNola, A. & Haak, J.R. Molecular dynamics with coupling to an external bath. *The Journal of Chemical Physics* **81**, 3684-3690 (1984).
77. Ryckaert, J.-P., Ciccotti, G. & Berendsen, H.J.C. Numerical integration of the cartesian equations of motion of a system with constraints: molecular dynamics of n-alkanes. *Journal of Computational Physics* **23**, 327-341 (1977).
78. Miyamoto, S. & Kollman, P.A. Settle: An analytical version of the SHAKE and RATTLE algorithm for rigid water models. *Journal of Computational Chemistry* **13**, 952-962 (1992).
79. Michaud-Agrawal, N., Denning, E.J., Woolf, T.B. & Beckstein, O. MDAnalysis: A toolkit for the analysis of molecular dynamics simulations. *Journal of Computational Chemistry* **32**, 2319-2327

(2011).

80. R Core Team (R Foundation for Statistical Computing, Vienna, Austria; 2017).

81. Rohart, F., Gautier, B., Singh, A. & Lê Cao, K.-A. mixOmics: An R package for 'omics feature selection and multiple data integration. *PLOS Computational Biology* **13**, e1005752 (2017).

984 **Figure Legends**

985 **Figure 1. The yeast PPAT Ade4 concentrates in fine particles**

986 A. Schematic of purine *de novo* and salvage pathways.

987 B. Fluorescent images of cells expressing Ade4 tagged C-terminally with the indicated
988 green fluorescent protein. Cells were grown in medium containing 0.02 mg/ml adenine,
989 washed with medium with or without adenine, and then incubated in the same medium
990 for 45 min before imaging. The intensity of GFP is represented by an inverted grayscale.
991 Dotted lines indicate the cell outline.

992 C. Quantification of the mean fluorescence intensity of Ade4 condensates observed in
993 cells as shown in (B). Data are represented by box and dot plots. Cross marks indicate the
994 population mean. *P*-values versus mGFP are shown (Steel's multiple comparison test).

995 D. A higher resolution image of Ade4-mNG particles. Z-positions are represented by a
996 color code (left). A grayscale image of particles (middle) and a bright field image of cells
997 (right) are also shown.

998 E. Time-lapse imaging of the assembly of Ade4-mNG particles by adenine depletion.
999 Cells were grown in medium containing 0.02 mg/ml adenine and washed with medium
1000 lacking adenine at t = 0 min.

1001 F. Time-lapse imaging of the disassembly of Ade4-mNG particles by adenine
1002 supplementation. Cells were grown in the absence of adenine and 0.02 mg/ml adenine
1003 was supplemented at t = 0 min.

1004 G, H. Panels G and H show the quantification of data in (E) and (F), respectively. The
1005 number of intracellular Ade4-mNG particles was counted as the number of maxima of
1006 green fluorescence intensity per cell. Data are the mean of 10-12 independent fields of
1007 view, and approximately 70 cells were examined per field. The shaded area indicates ±
1008 1SD.

1009 I-K. Closer time-lapse imaging of Ade4-mNG particles. A cell bearing the particles
1010 (outlined by a dotted line in the first frame) was imaged on a single z-plane at 1-s intervals.
1011 The intensity of mNG is represented by an inverted grayscale. Panel J shows a color-
1012 coded superimposition of the images from each frame shown in (I). Panel K is a
1013 kymograph of the images shown in (I). Arrowheads indicate the appearance of some
1014 particles. Scale bars = 5 μm.

1015

1016 **Figure S1. Additional data regarding the intracellular localization of Ade4. Related**
1017 **to Figure 1**

1018 A. Phase and RFP images of cells expressing Ade4 tagged C-terminally with the red
1019 fluorescent protein mKate2.

1020 B. A control experiment of time-lapse imaging of the assembly of Ade4-mNG particles
1021 by adenine depletion shown in Fig. 1E. Cells were grown in medium containing 0.02
1022 mg/ml adenine and washed with medium containing the same concentration of adenine
1023 at t = 0 min.
1024 C. A control experiment of time-lapse imaging of the disassembly of Ade4-mNG particles
1025 by adenine supplementation shown in Fig. 1F. Cells were grown in the absence of adenine
1026 and sterile water was supplemented instead of adenine at t = 0 min. Scale bars = 5 μm.
1027
1028 D-F. Another example of time-lapse imaging of Ade4-mNG particles, related to Fig. 1I-
1029 K. Experimental conditions and graph descriptions are the same as in Fig. 1I-K.
1030
1031
1032 **Figure 2. Ade4 condensate formation requires active TORC1 and ribosome**
1033 **biogenesis**
1034 A. The aliphatic alcohol 1,6–hexanediol dissolves Ade4 condensates. Wild-type cells
1035 harboring Ade4-mNG condensates were treated with 2 μg/ml digitonin ± 10% (w/v) 1,6-
1036 hexanediol for 10 min and then imaged.
1037 B. Quantification of data shown in (A). The percentage of cells with Ade4-mNG
1038 condensates per field of view (containing 361 ± 159 cells) was plotted. Data were pooled
1039 from three independent experiments. Bars and error bars indicate the mean ± 1SD. *P*-
1040 values were calculated using the two-tailed Steel-Dwass multiple comparison test.
1041 C. Domain structures of the budding yeast Ade4 and the IDR mutant. The bottom graph
1042 shows disorder predictions.
1043 D. The C-terminal IDR of Ade4 is required for condensate formation. Cells expressing
1044 the mutant Ade4 lacking the C-terminal IDR tagged with mNG were incubated in the
1045 absence of purine bases for 45 min and imaged.
1046 E. Wild-type and *fpr1*Δ cells expressing Ade4-GFP were grown in medium without
1047 adenine in the presence of 0.02% (v/v) DMSO or 0.02% DMSO plus 2 μg/ml rapamycin
1048 for 45 min before imaging.
1049 F. Rapamycin suppresses the assembly of Ade4-mNG condensates. Wild-type cells
1050 expressing Ade4-mNG were treated with rapamycin and imaged as described in (E).
1051 G. Quantification of data shown in (F). The percentage of cells with Ade4-mNG
1052 condensates per field of view (containing 443 ± 138 cells) was plotted. Data were pooled
1053 from two independent experiments. Bars and error bars indicate the mean ± 1SD. *P*-
1054 values were calculated using the two-tailed Mann-Whitney U test.
1055 H. The assembly of Ade4-mNG condensates was significantly suppressed in *sfp1*Δ and

1056 *sit4*Δ cells.
1057 I. Quantification of data shown in (H). The percentage of cells with Ade4-mNG
1058 condensates per field of view (containing 517 ± 123 cells) was plotted. Data were pooled
1059 from three independent experiments. Bars and error bars indicate the mean ± 1SD. *P*-
1060 values versus wt were calculated using the two-tailed Steel's multiple comparison test.
1061 J. The inhibition of ribosome synthesis suppresses the assembly of Ade4 condensates.
1062 Cells expressing Ade4-GFP were grown in medium containing adenine and then
1063 incubated in medium without adenine in the presence of 0.05% (v/v) DMSO or 0.05%
1064 DMSO plus 5 μg/ml diazaborine for 45 min before imaging. The percentage of cells with
1065 Ade4-GFP foci per field of view (containing 780 ± 214 cells) was plotted. Data were
1066 pooled from two independent experiments. Bars and error bars indicate the mean ± 1SD.
1067 *P*-values were calculated using the two-tailed Mann-Whitney U test. Representative cell
1068 images are shown in Figure S3C. Scale bars = 5 μm.
1069
1070 **Figure S2. The IDR is conserved in PPATs of various species**
1071 A. The C-terminal IDR is conserved in PPATs of Ascomycota. Heatmap showing the
1072 disorder scores of PPAT amino acid sequences of 81 ascomycota.
1073 B. Heatmap showing the disorder scores of PPAT amino acid sequences of 100 organisms,
1074 including 19 ascomycota. Phylogenetic groups are color-coded on the left.
1075 C-D. Amino acid sequences of IDTs vary across species. Multiple amino acid sequence
1076 alignment of the C-terminal region of PPAT. In (C), three fungi and 13 representative
1077 organisms from the following groups are selected: archaea, bacteria, protozoa, plants,
1078 nematodes, insects, echinoidea, fish, amphibians, mammals, reptiles, birds, and ascidians.
1079 In (D), 13 species are selected from ascomycota. Green boxes indicate the region
1080 corresponding to the C-terminal IDR of Ade4.
1081
1082 **Figure S3. Formation of Ade4 condensates in TORC1-related mutants. Related to**
1083 **Figure 2.**
1084 A. Assembly of Ade4-GFP foci in single gene deletion mutants of the upstream regulator
1085 and downstream effector of TORC1 signaling. Cells of the indicated genotype expressing
1086 Ade4-GFP were grown in medium containing adenine and then incubated in medium
1087 without adenine for 45 min before imaging.
1088 B. Summary of the percentage of cells showing Ade4-GFP foci in the wild-type and 37
1089 single-gene deletion mutants. The percentage of cells with Ade4-GFP foci per field of
1090 view was plotted. Data were pooled from 2-3 independent experiments. Bars and error
1091 bars indicate the mean ± 1SD.

1092 C. The inhibition of ribosome synthesis suppressed the assembly of Ade4-GFP foci.
1093 Related to Figure 2J.
1094 D. The inhibition of ribosome synthesis suppressed the assembly of Ade4-mNG
1095 condensates. Cells expressing Ade4-mNG were grown in medium containing adenine and
1096 then incubated in medium without adenine in the presence of 0.05% (v/v) DMSO or
1097 0.05% DMSO plus 5 μg/ml diazaborine for 45 min before imaging. Scale bars = 5 μm.
1098
1099 **Figure 3. The Ade4 protein condensates into particles under molecular crowding**
1100 **conditions *in vitro***
1101 A. Purified Ade4-mNG condensated into fine particles in a PEG concentration-dependent
1102 manner. Ade4-mNG (0.15 μM) was supplemented with PEG8000 at the indicated
1103 concentration (%, w/v). Inverted grayscale images are shown.
1104 B-C. Quantification of data shown in (A). The mean fluorescence intensities of Ade4-
1105 mNG particles were box plotted in (B). Cross marks indicate the population mean. The
1106 integrated fluorescence intensities of particles were summed per field and plotted in (C).
1107 Bars and error bars indicate the mean ± 1SD. Seven to 10 fields of view were imaged for
1108 each condition and an average of 390 particles per field were examined. *P*-values were
1109 calculated using the two-tailed Steel-Dwass multiple comparison test.
1110 D. 1,6-Hexanediol attenuated the *in vitro* condensation of Ade4-mNG. Ade4-mNG (0.15
1111 μM) was supplemented with 10% PEG8000 in the presence of 0 or 10% (w/v) 1,6-
1112 hexanediol. Fluorescence intensity is represented by pseudo-colors.
1113 E-F. Quantification of data shown in (D). The mean fluorescence intensities of particles
1114 were box plotted in (E). Cross marks indicate the population mean. The integrated
1115 fluorescence intensities of particles were summed per field and plotted in (F). Bars and
1116 error bars indicate the mean ± 1SD. Ten fields of view were imaged for each condition,
1117 and an average of 1197 particles per field were examined. *P*-values were calculated using
1118 the two-tailed Mann-Whitney U test (E) or Welch's *t*-test (F).
1119 G. Ade4ΔIDR-mNG condensated into particles less effectively than Ade4-mNG *in vitro*.
1120 The supplementation of 0.2 μM Ade4-mNG or Ade4ΔIDR-mNG with 10% PEG8000 was
1121 performed. Fluorescence intensity is represented by pseudo-colors.
1122 H-I. Quantification of data shown in (G). The mean fluorescence intensities of particles
1123 were box plotted in (H). Cross marks indicate the population mean. The integrated
1124 fluorescence intensities of particles were summed per field and plotted in (I). Bars and
1125 error bars indicate the mean ± 1SD. Twenty-eight fields of view were imaged for each
1126 condition, and an average of 1341 particles per field were examined. *P*-values were
1127 calculated using the two-tailed Mann-Whitney U test. Scale bars = 5 μm.

1128

1129 **Figure S4. Purification and basic characterization of the Ade4 protein *in vitro***

1130 A. Purified proteins used in the present study. Proteins were resolved by SDS-PAGE and
1131 stained with FastGene™ Q-stain.

1132 B. The purified mNG protein did not condensate into particles even under molecular
1133 crowding conditions. The supplementation of 0.14 μM mNG with 0 or 10% PEG8000
1134 was performed.

1135 C. The *in vitro* condensation of Ade4-mNG depends on the size of PEG. The
1136 supplementation of 0.15 μM Ade4-mNG with 10% PEG of the indicated average
1137 molecular weight was performed.

1138 D-E. Quantification of data shown in (C). The mean fluorescence intensities of Ade4-
1139 mNG particles were box plotted in (D). Cross marks indicate the population mean. The
1140 integrated fluorescence intensities of particles were summed per field and plotted in (E).
1141 Bars and error bars indicate the mean ± 1SD. Seven to 8 fields of view were imaged for
1142 each condition, and an average of 399 particles per field were examined. *P*-values were
1143 calculated using the two-tailed Steel-Dwass multiple comparison test.

1144 F. Condensation of Ade4-mNG into particles with crowding agents other than PEG. The
1145 supplementation of 0.14 μM Ade4-mNG with the indicated crowding agents was
1146 performed. Scale bars = 5 μm.

1147

1148 **Figure S5. Estimation of the intracellular concentration of Ade4.**

1149 Data regarding the protein abundance of the budding yeast Ade4 were downloaded from
1150 the Saccharomyces Genome Database
1151 (https://www.yeastgenome.org/locus/S000004915/protein). Data were derived from
1152 twenty quantitative genome-wide proteomic studies and normalized to a unit of molecules
1153 per cell. These values were converted to micromoles assuming that the average
1154 cytoplasmic volume of the haploid yeast cell was 42 fL[68]. Data were classified according
1155 to the measuring methods (flow cytometry, quantitative fluorescence microscopy,
1156 immunoblotting, and mass spectrometry) and the type of medium (rich or synthetic) and
1157 were then plotted. Bars and error bars indicate the mean ± 1SD.

1158

1159 **Figure 4. Metabolomics analysis of budding yeast cells grown in the absence and**
1160 **presence of adenine**

1161 A. Experimental scheme for adenine exposure and cell quenching. The preculture was
1162 inoculated into the main culture at 0 h.

1163 B. Sparse PLS-DA of metabolome samples. A 2D score plot of the first two components

with ellipse plots (95% confidence level).

C. Clustered heatmap of significantly changed metabolites. Rows indicate 56 metabolites that changed significantly between the indicated conditions (FDR-adjusted *p*-value <0.05). Columns represent seven independent samples for each condition. Values for each metabolite were converted to Z-scores and plotted. Metabolites were clustered using the complete linkage method and Euclidean distance measure.

D. Changes in purine nucleotides and their derivatives. Data on the indicated metabolites were converted to fold change (FC) relative to the mean at 0 h (in the absence of adenine) and plotted. Bars and error bars indicate the mean ± 1SD calculated from 7 independent biological replicates for each condition. The color of the bar indicates whether the change in the metabolite was significant.

E. Correlation coefficients of the top 25 metabolites correlated with intracellular adenine. Some metabolites of interest are indicated with arrows.

Figure S6. Additional data regarding the metabolomics analysis. Related to Figure 4

A. Changes in the indicated metabolites. Experimental conditions and graph descriptions are the same as in Fig. 4D.

B. The intracellular concentration of PRPP decreases in the presence of environmental adenine. The amount of PRPP in each sample was converted to an intracellular concentration and plotted. *P*-values were calculated using the two-tailed Tukey-Kramer's multiple comparison test.

Figure 5. Intracellular derivatives of purine nucleotides regulate the formation of Ade4 condensates

A. *De novo* and salvage pathways for purine synthesis in budding yeast.

B. Assembly of Ade4-GFP foci in purine metabolism mutants. Cells with Ade4-GFP foci in the absence of purine bases (mock) were treated with the same medium or medium containing 20 μg/ml adenine (+adenine) or 25 μg/ml hypoxanthine (+hypoxanthine) for 20 min and then imaged. Simplified views of the metabolism of the incorporated purine bases in the strains are shown.

C-E. Quantification of data shown in (B). The percentage of cells with foci per field of view was quantified and plotted. Bars and error bars indicate the mean ± 1SD. Data were pooled from 2-3 independent experiments, and more than 16 fields of view were imaged for each condition. *P*-values versus the mock were calculated using the two-tailed Steel's multiple comparison test: *, $p < 0.01$; ***, $p < 10^{-10}$. Scale bar = 5 μm.

1200

1201 **Figure S7. Alanosine inhibits the dissolution of Ade4 foci in the presence of**
1202 **hypoxanthine. Related to Figure 5.**
1203 A. Alanosine inhibits the adenylosuccinate synthetase ADE12.
1204 B. Assembly of Ade4-GFP foci in the presence of alanosine. Cells expressing Ade4-GFP
1205 were incubated in medium lacking adenine in the presence of 0 (mock) or 30 μg/ml
1206 alanosine (+alanosine) for 40 min to allow for the assembly of Ade4-GFP foci and were
1207 then imaged (SC). Cells were further treated with the same medium supplemented with
1208 24 μg/ml hypoxanthine for 15 min and then imaged again (SC + hyp). Scale bar = 5 μm.
1209 C. Quantification of data shown in (B). The percentage of cells with foci per field of view
1210 (containing 182 ± 46 cells) was quantified and plotted. Data were pooled from two
1211 independent experiments. Bars and error bars indicate the mean ± 1SD. The significance
1212 of differences was tested using the unpaired two-tailed Welch's *t*-test. *P*-values versus the
1213 mock are shown.
1214

1215 **Figure 6. Purine nucleotides attenuate the assembly of Ade4 condensates *in vitro***
1216 A. Effects of purine nucleotides on the *in vitro* assembly of Ade4 condensates. Ade4-
1217 mNG (0.2 μM) was supplemented with 10% PEG8000 in the presence of the indicated
1218 purine nucleotide. Fluorescence intensity is represented by pseudo-colors. Scale bars = 5
1219 μm.
1220 B. Quantification of data shown in (A). The integrated fluorescence intensities of
1221 condensates were summed per field and plotted. Bars and error bars indicate the mean ±
1222 1SD. Between 23 and 28 fields of view were imaged for each condition from two
1223 independent preparations, and an average of 1323 particles per field were examined. *P*-
1224 values were calculated using the two-tailed Tukey-Kramer's multiple comparison test.
1225 C. The supplementation of 0.2 μM Ade4-mNG with 10% PEG8000 was performed in the
1226 presence of the indicated concentration of AMP. The integrated fluorescence intensities
1227 of the condensates were summed per field, normalized to the mean at 0 μM, and plotted.
1228 Bars and error bars indicate the mean ± 1SD. From 4 independent preparations, 41-55
1229 fields of view were imaged for each condition, and an average of 1200 particles per field
1230 were examined. *P*-values were calculated using the two-tailed Steel's multiple
1231 comparison test.
1232 D. Effects of AMP on the *in vitro* assembly of Ade4 and Ade4ΔIDR condensates. The
1233 supplementation of 0.2 μM Ade4-mNG (FL) or Ade4ΔIDR-mNG (ΔIDR) with 10%
1234 PEG8000 was performed in the presence of 0 or 500 μM AMP. The integrated
1235 fluorescence intensities of condensates were summed per field, normalized to the mean

1236 of FL at 0 μM AMP, and plotted. Bars and error bars indicate the mean ± 1SD. Between
1237 40 and 45 fields of view were imaged for each condition from 3 independent preparations.
1238 *P*-values were calculated using the two-tailed Welch's *t*-test.
1239
1240 **Figure S8. Additional data regarding the assembly of Ade4 condensates *in vitro*,**
1241 **related to Figure 6.**
1242 A, B. Effects of purine base derivatives on the *in vitro* assembly of Ade4 condensates.
1243 The supplementation of 0.2 μM Ade4-mNG with 10% PEG8000 was performed in the
1244 presence of the indicated compound. Glucose (Glu) was used as a negative control. The
1245 integrated fluorescence intensities of condensates were summed per field and plotted in
1246 (A). The mean fluorescence intensities of Ade4-mNG condensates were averaged per
1247 field and plotted in (B). Bars and error bars indicate the mean ± 1SD. Twenty fields of
1248 view were imaged for each condition from two independent preparations, and an average
1249 of 1452 particles per field were examined. *P*-values were calculated using the two-tailed
1250 Steel's multiple comparison test. Glu, glucose; Ade, adenine; Ino, inosine; d-Ino, deoxy-
1251 inosine.
1252 C. Effects of purine nucleotides on the *in vitro* assembly of Ade4 condensates. Data were
1253 from the same experiment shown in Figure 6A. The mean fluorescence intensities of
1254 Ade4-mNG condensates were averaged per field and plotted. Bars and error bars indicate
1255 the mean ± 1SD. *P*-values were calculated using the two-tailed Tukey-Kramer's multiple
1256 comparison test.
1257 D-F. The supplementation of 0.2 μM Ade4-mNG with 10% PEG8000 was performed in
1258 the presence of the indicated concentrations of ADP (D), ATP (E), and GMP (F). The
1259 integrated fluorescence intensities of the condensates were summed per field, normalized
1260 to the mean at 0 μM, and plotted. Bars and error bars indicate the mean ± 1SD. From two
1261 independent preparations, 25-31 fields of view were imaged for each condition, and an
1262 average of 1200 particles per field were examined. *P*-values were calculated using the
1263 two-tailed Steel's multiple comparison test.
1264 G-H. Inhibitory effect of SAH on the *in vitro* condensation of Ade4-mNG. The
1265 supplementation of 0.2 μM Ade4-mNG with 10% PEG8000 was performed in the
1266 presence of 0.5% (v/v) DMSO and 500 μM SAH or AMP and imaged. The average
1267 fluorescence intensities (G) and integrated fluorescence intensities (H) of the particles
1268 summed per field were normalized to the mean of the DMSO alone and plotted. Bars and
1269 error bars indicate the mean ± 1SD. From 4 independent preparations, 53-57 fields of
1270 view were imaged for each condition. The *p*-values were calculated using the two-tailed
1271 Dunnett's multiple comparison test.

1272

1273 **Figure 7. PRPP facilitates the assembly of Ade4 condensates**

1274 A. PRPP augments the *in vitro* assembly of Ade4 condensates. The supplementation of
1275 0.2 μM Ade4-mNG with 10% PEG8000 was performed in the presence of the indicated
1276 concentration of PRPP. The integrated fluorescence intensities of the condensates were
1277 summed per field and plotted. Throughout the figure, bars and error bars indicate the
1278 mean ± 1SD. From 2 independent preparations, 29-31 fields of view were imaged for
1279 each condition, and an average of 1200 particles per field were examined. *P*-values were
1280 calculated using the two-tailed Steel's multiple comparison test.

1281 B, C. PRPP promotes the formation of Ade4 condensates *in vitro* at suboptimal PEG
1282 concentrations. In the presence of 100 or 0 μM PRPP, 0.2 μM Ade4-mNG was
1283 supplemented with PEG8000 at the indicated concentration and imaged. The integrated
1284 fluorescence intensities of the condensates were summed per field and plotted in (B).
1285 From 2 independent preparations, 19-24 fields of view were imaged for each condition.
1286 ND, not determined. Representative images at 7.5% PEG are shown in (C).

1287 D, E. PRPP antagonizes the inhibitory effects of AMP. In the presence of 0 or 1 mM AMP
1288 and the indicated concentrations of PRPP, 0.2 μM Ade4-mNG was supplemented with
1289 7.5% or 10% PEG8000. The integrated fluorescence intensities of the condensates were
1290 summed per field, normalized to the mean of the mock control (no AMP and no PRPP),
1291 and plotted in (D). From 2 independent preparations, 21-27 fields of view were imaged
1292 for each condition. *P*-values were calculated using the two-tailed Steel's multiple
1293 comparison test. Representative images at 7.5% PEG are shown in (E).

1294 F. Interactions between a PRPP analog and specific amino acid residues in the PRPP
1295 binding motif in the *E. coli* PPAT (pdb file: 1ecc). The dotted line indicates a hydrogen
1296 bond.

1297 G. PRPP and purine nucleotides (*e.g.*, AMP) interact competitively with the binding motif.
1298 Purine nucleotides may also interact with additional binding site(s) and inhibit Ade4
1299 condensation. See the text for details.

1300 H. The interaction of Ade4 with PRPP is important for condensate assembly. Ade4-mNG
1301 (WT) and Ade4-D373A/D374A-mNG (DA) cells were incubated in the absence of purine
1302 bases for 45 min and imaged. The percentages of cells with condensates per one field of
1303 view were quantified and plotted. Data were pooled from 2 independent experiments, and
1304 more than 16 fields of view were imaged for each condition. *P*-values were calculated
1305 using the two-tailed Mann-Whitney U test. A representative image of mutant cells is
1306 shown.

1307 I. PRPP did not stimulate the condensate assembly of the DA mutant. The

1308 supplementation of 0.2 μM Ade4-mNG (WT) and Ade4-D373A/D374A-mNG (DA) with
1309 7.5% PEG8000 was performed in the presence of 0 or 100 μM PRPP and imaged. The
1310 integrated fluorescence intensities of the condensates were summed per field, normalized
1311 to the mean at 0 μM PRPP (dotted line), and plotted. From 2 independent preparations,
1312 >22 fields of view were imaged for each condition. *P*-values were calculated using the
1313 two-tailed Welch's *t*-test.
1314 J. The DA mutant is less sensitive to the inhibitory effects of AMP. The supplementation
1315 of 0.2 μM Ade4-mNG (WT) and Ade4-D373A/D374A-mNG (DA) with 10% PEG8000
1316 was performed in the presence of 0 or 1 mM AMP and imaged. The integrated
1317 fluorescence intensities of the condensates were summed per field, normalized to the
1318 mean at 0 mM AMP (dotted line), and plotted. From 2-3 independent preparations, >24
1319 fields of view were imaged for each condition. *P*-values were calculated using the two-
1320 tailed Mann-Whitney U test.
1321 K. PRPP did not antagonize AMP in the condensate formation of the DA mutant. In the
1322 presence of 0 or 1 mM AMP and the indicated concentrations of PRPP, 0.2 μM Ade4-
1323 D373A/D374A-mNG was supplemented with 7.5% or 10% PEG8000. The integrated
1324 fluorescence intensities of the condensates were summed per field, normalized to the
1325 mean of the mock control (no AMP and no PRPP), and plotted. From 2 independent
1326 preparations, 22-25 fields of view were imaged for each condition. *P*-values were
1327 calculated using the two-tailed Steel's multiple comparison test. Scale bars = 5 μm.
1328
1329 **Figure S9. Effects of IMP on the assembly of Ade4 condensates *in vitro***
1330 A-B. IMP did not affect the *in vitro* condensation of Ade4-mNG. The supplementation of
1331 0.2 μM Ade4-mNG with 10% PEG8000 was performed in the presence of 500 μM IMP
1332 or AMP. The average fluorescence intensities (A) and integrated fluorescence intensities
1333 (B) of the condensates summed per field were normalized to the mean of the mock, and
1334 plotted. Bars and error bars indicate the mean ± 1SD. From 4 independent preparations,
1335 62-72 fields of view were imaged for each condition. *P*-values were calculated using the
1336 two-tailed Steel's multiple comparison test.
1337
1338 **Figure S10. PRPP facilitates the assembly of Ade4 condensates, related to Figure 7**
1339 A. PRPP augments the *in vitro* assembly of Ade4 condensates. Data were from the same
1340 experiment shown in Figure 7A. The mean fluorescence intensities of Ade4-mNG
1341 condensates were averaged per field and plotted. Throughout the figure, bars and error
1342 bars indicate the mean ± 1SD. *P*-values were calculated using the two-tailed Steel's
1343 multiple comparison test.

1344 B, C. PRPP promotes the formation of Ade4 condensates *in vitro* at suboptimal PEG
1345 concentrations. Data were from the same experiment shown in Figure 7B, C. The mean
1346 fluorescence intensities of Ade4-mNG condensates were averaged per field and plotted
1347 in (B). ND, not determined. Representative images at 5% PEG are shown in (C).
1348 D. PRPP antagonizes the inhibitory effects of AMP. Data were from the same experiment
1349 shown in Figure 7D-E. The mean fluorescence intensities of Ade4-mNG condensates
1350 were averaged per field, normalized to the mean of the mock control (no AMP and no
1351 PRPP), and plotted. *P*-values were calculated using the two-tailed Steel's multiple
1352 comparison test.
1353 E. The amino acid residues of the PRPP binding motif in PPAT are well conserved among
1354 species.
1355 F. Interactions between an AMP and specific amino acid residues in the PRPP binding
1356 motif in the *E. coli PPAT* (pdb file: 1ecj). The dotted line indicates a hydrogen bond.
1357 G. The purified Ade4-D373A/D374A-mNG (Ade4-DA-mNG) protein. Proteins were
1358 resolved by SDS-PAGE and stained with FastGene™ Q-stain.
1359 H. Ade4-DA-mNG condensated into particles under molecular crowding conditions. The
1360 supplementation of 0.2 μM Ade4-mNG (WT) and Ade4-DA-mNG (DA) with 10%
1361 PEG8000 was performed and imaged. The integrated fluorescence intensities of the
1362 condensates were summed per field and plotted. From 2 independent preparations, >36
1363 fields of view were imaged for each condition. *P*-values were calculated using the two-
1364 tailed Mann-Whitney U test.
1365 I, J. PRPP did not antagonize AMP in the condensate formation of the DA mutant. Data
1366 were from the same experiment shown in Figure 7K. The mean fluorescence intensities
1367 of Ade4-D373A/D374A-mNG condensates were averaged per field, normalized to the
1368 mean of the mock control (no AMP or PRPP), and plotted in (I). *P*-values were calculated
1369 using the two-tailed Steel's multiple comparison test. Representative images at 7.5% PEG
1370 are shown in (J). Scale bars = 5 μm.
1371
1372 **Figure 8. MD calculations predict the possible condensation-dependent activation of**
1373 **PPAT by enabling intermolecular substrate channeling**
1374 A. Reaction formulae corresponding to the glutamine-dependent PRA synthesis (Gln-
1375 PRA activity) and NH_3-dependent PRA synthesis (NH_3-PRA activity) of PPAT.
1376 B. Reaction mechanisms suggested in a previous study.
1377 C. Intramolecular and intermolecular channeling of glutamine-derived NH_3.
1378 D, E, H. Time series for the dihedral angle of the Phe260 side chain and the distance of
1379 NH_3 from the initial structure (D: holo; E: semi-holo; and H: R333A mutant). Moving

1380 averages are plotted in bold lines. Under each condition, 300-ns simulations were
1381 performed ten times individually. The blue backgrounds indicate the open state of the
1382 Phe260 sidechain. The schematic diagram shows the state of the Arg gate and the
1383 movement of the NH_3 molecule.
1384 F. The hydrophobic (orange) and front (red) channels of *E. coli* PPAT.
1385 G. The conserved Arg residue functions as a gate of the front channel. Top: a structural
1386 snapshot around the Arg gate. Bottom: a scheme of the Arg gate. Hydrogen bonds are
1387 shown as red dotted lines.
1388 I. The reaction mechanisms suggested in the present study.
1389
1390 **Figure S11. Possible enzymatic reaction pathways of PPAT**
1391 A. Intramolecular channeling of glutamine-derived NH_3 proposed by Krahn et al.[34].
1392 B. Mechanism of NH_3-dependent activity proposed by Chen et al.[53]. External NH_3 enters
1393 the channel from the glutamine site irrespective of glutamine binding.
1394 C. The MD simulation in the present study suggests that glutamine-derived NH_3 leaks
1395 through the front channel following the attack of exogenous NH_3.
1396 D. Condensation-dependent activation of Ade4 proposed by the present study. Glutamine-
1397 derived NH_3 leaked from the front channel rapidly diffuses away. In the Ade4 condensate,
1398 the opportunity for NH_3 to be captured by other molecules and further reacted with PRPP
1399 will increase. This activation may be described as intermolecular NH_3 channeling. PRPP
1400 is not depicted in the schema.
1401
1402 **Figure 9. The formation of Ade4 condensates is important for efficient *de novo***
1403 **purine synthesis during cell growth**
1404 A. Growth of ADE4-3HA and ADE4ΔIDR-3HA cells on solid media. Cells of each strain
1405 were spotted on medium containing the indicated concentration of ammonium sulfate
1406 (AS), and then grown at 30°C for 2-3 days.
1407 B. Immunoblot analysis of the protein level of Ade4. Total cell extracts were prepared
1408 from cells expressing the indicated Ade4 construct. Ade4-3HA and Ade4ΔIDR-3HA were
1409 detected as approximately 60-kDa bands by an anti-HA antibody. The bands of GAPDH
1410 are shown as a loading control.
1411 C. Growth curves of Ade4-3HA and Ade4ΔIDR-3HA cells in liquid media without
1412 adenine. Cells were grown at 30°C for 40 h in medium containing the indicated
1413 concentration of ammonium sulfate (AS) in the absence or presence of adenine. Data are
1414 the mean of 6 replicates, and the shaded area indicates ± 1SD.
1415 D. Quantification of data shown in (C). The time to half-maximum density

1416 (corresponding to normalized OD_{595} = 0.5) was calculated and plotted. Bars and error
1417 bars indicate the mean ± 1SD. *P*-values were calculated using the two-tailed Welch's *t*-
1418 test.
1419
1420
1421 **Figure 10. Molecular crowding and interactions with effectors regulate Ade4**
1422 **condensation**
1423 A schematic model showing the regulation of Ade4 condensation proposed in the present
1424 study. See the text for details.
1425

Supplemental Information

Captions for supplementary data

Data S1. Metabolomics profile of budding yeast cells grown in the absence and presence of adenine. The normalized peak area is the signal peak area corrected by the total ion chromatogram. Each group contains seven biological replicates. All data of the normalized peak area were subjected to sparse PLS-DA shown in Fig. 4B. Means and standard deviations (SD) across replicates are shown as a reference. *P*-values of the one-way ANOVA and FDR-adjusted *p*-values were calculated using MetaboAnalyst 6.0. Blue bold values indicate less than 0.05.

Data S2. Metabolic profile of 56 metabolites whose concentrations were significantly changed by adenine. Each group contains seven biological replicates. Values are the normalized peak area further converted to Z-scores across samples. Data were subjected to the heatmap analysis shown in Fig. 4C.

Data S3. Changes in purine nucleotides and their derivatives, related to Figs. 4D and S6A. Each group contains seven biological replicates. Data were converted to fold change (FC) relative to the mean at 0 h (in the absence of adenine).

1446 Captions for supplementary movies

1447 **Movie S1**

1448 Time-lapse imaging of the assembly of Ade4-mNG condensates by adenine depletion.
1449 Cells were grown in medium containing 0.02 mg/ml adenine and washed with medium
1450 lacking adenine at t = 0 min. The three cells in the upper right are shown in Fig. 1E. Scale
1451 bar = 5 μm.

1452

1453 **Movie S2**

1454 Another example of cells showing the assembly of Ade4-mNG condensates by adenine
1455 depletion. Experimental conditions are the same as in Movie S1. Scale bar = 5 μm.

1456

1457 **Movie S3**

1458 A control experiment of time-lapse imaging of the assembly of Ade4-mNG condensates
1459 by adenine depletion. Cells were grown in medium containing 0.02 mg/ml adenine and
1460 washed with medium containing the same concentration of adenine at t = 0 min. The
1461 rightmost cell is shown in Fig. S1B. Scale bar = 5 μm.

1462

1463 **Movie S4**

1464 Time-lapse imaging of the disassembly of Ade4-mNG condensates by adenine
1465 supplementation. Cells were grown in the absence of adenine and 0.02 mg/ml adenine
1466 was supplemented at t = 0 min. The four cells in the upper left are shown in Fig. 1F. Scale
1467 bar = 5 μm.

1468

1469 **Movie S5**

1470 A control experiment of time-lapse imaging of the disassembly of Ade4-mNG
1471 condensates by adenine supplementation. Cells were grown in the absence of adenine and
1472 sterile water was supplemented in place of adenine at t = 0 min. The two cells in the center
1473 are shown in Fig. S1C Scale bar = 5 μm.

1474

1475 **Movie S6**

1476 Another example of cells showing Ade4-mNG condensates after a mock treatment with
1477 adenine. Experimental conditions are the same as in Movie S5. Scale bar = 5 μm.

1478

1479 **Movie S7**

1480 A close examination of the motility of Ade4-mNG condensates. Another example of data
1481 shown in Fig. 1I. Cells bearing condensates were imaged on a single z-plane at 1-s

1482 intervals. The intensity of mNG is represented by an inverted grayscale. Scale bar = 5 μm.
1483
1484 **Movie S8**
1485 Time-lapse video of the MD simulation of NH_3 and PPAT molecules in the semi-holo
1486 state, related Fig. 8E. This movie was created from MD snapshots during the simulation.
1487 The state of the Arg gate is also indicated. In this example, NH_3 was eventually released
1488 through the front channel (indicated by a circle).
1489
1490

Figure 1: The yeast PPAT Ade4 concentrates in fine particles

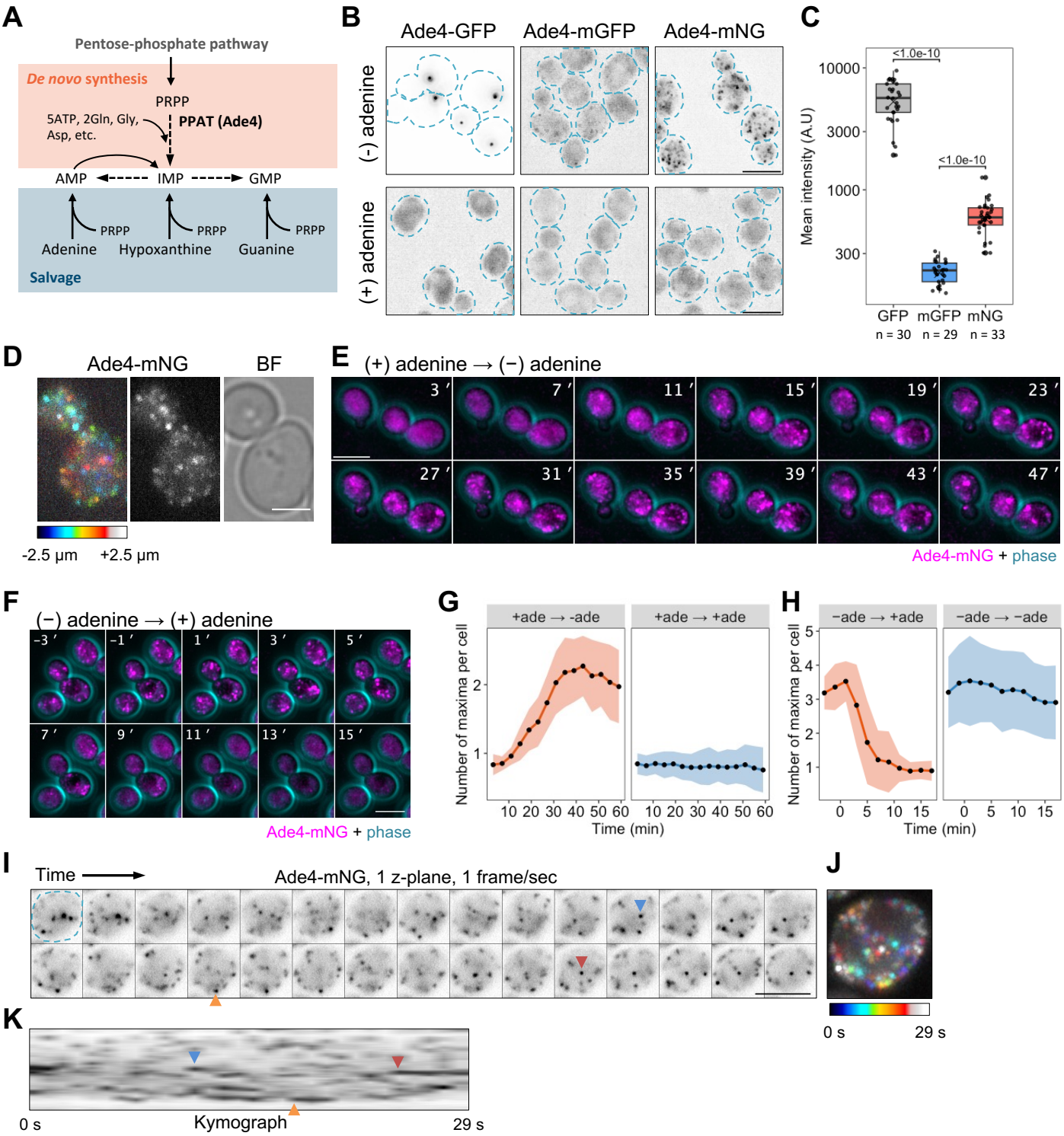

Figure S1: Additional data regarding the intracellular localization of Ade4. Related to Figure 1

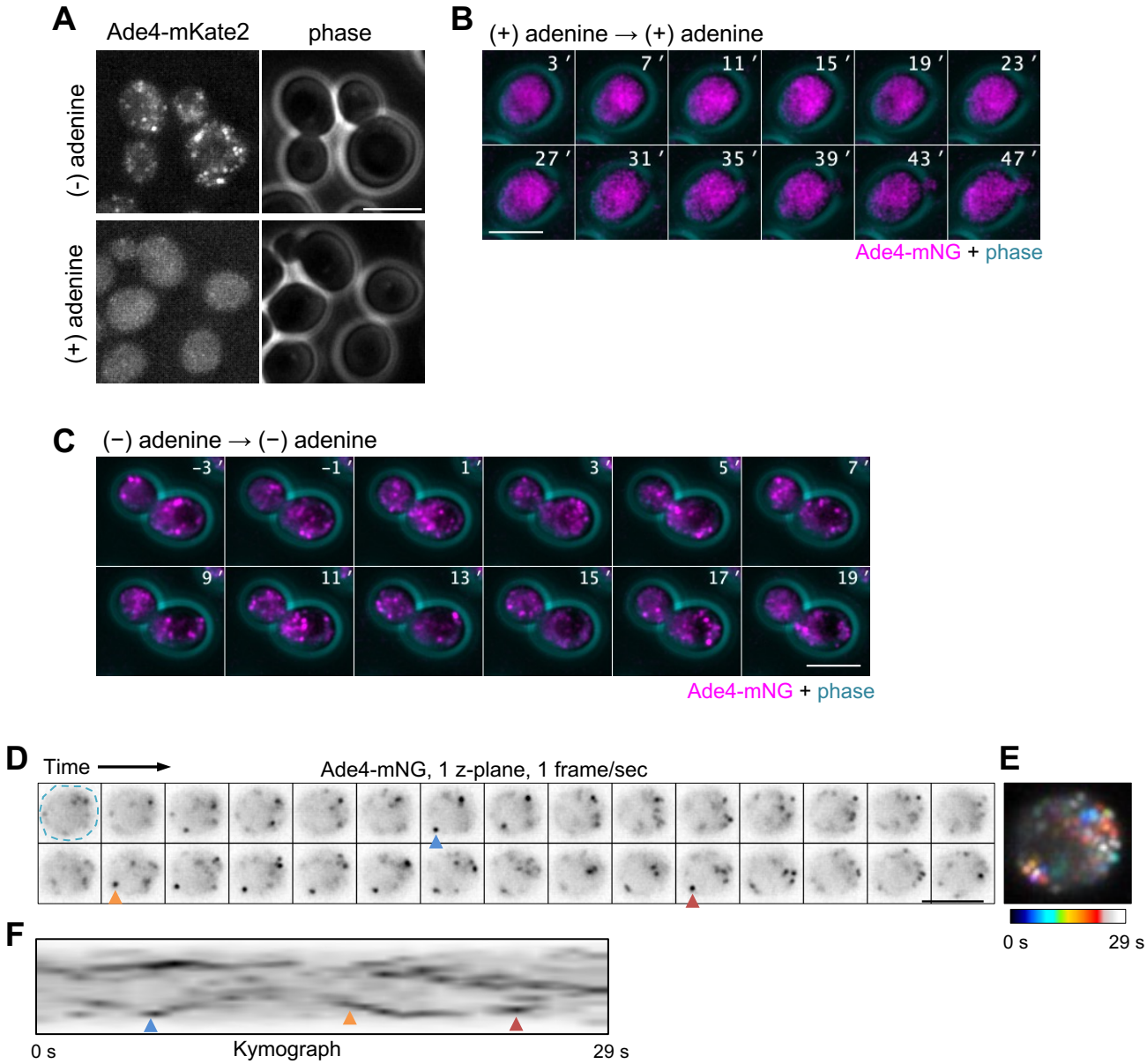

Figure 2: Ade4 condensate formation requires active TORC1 and ribosome biogenesis

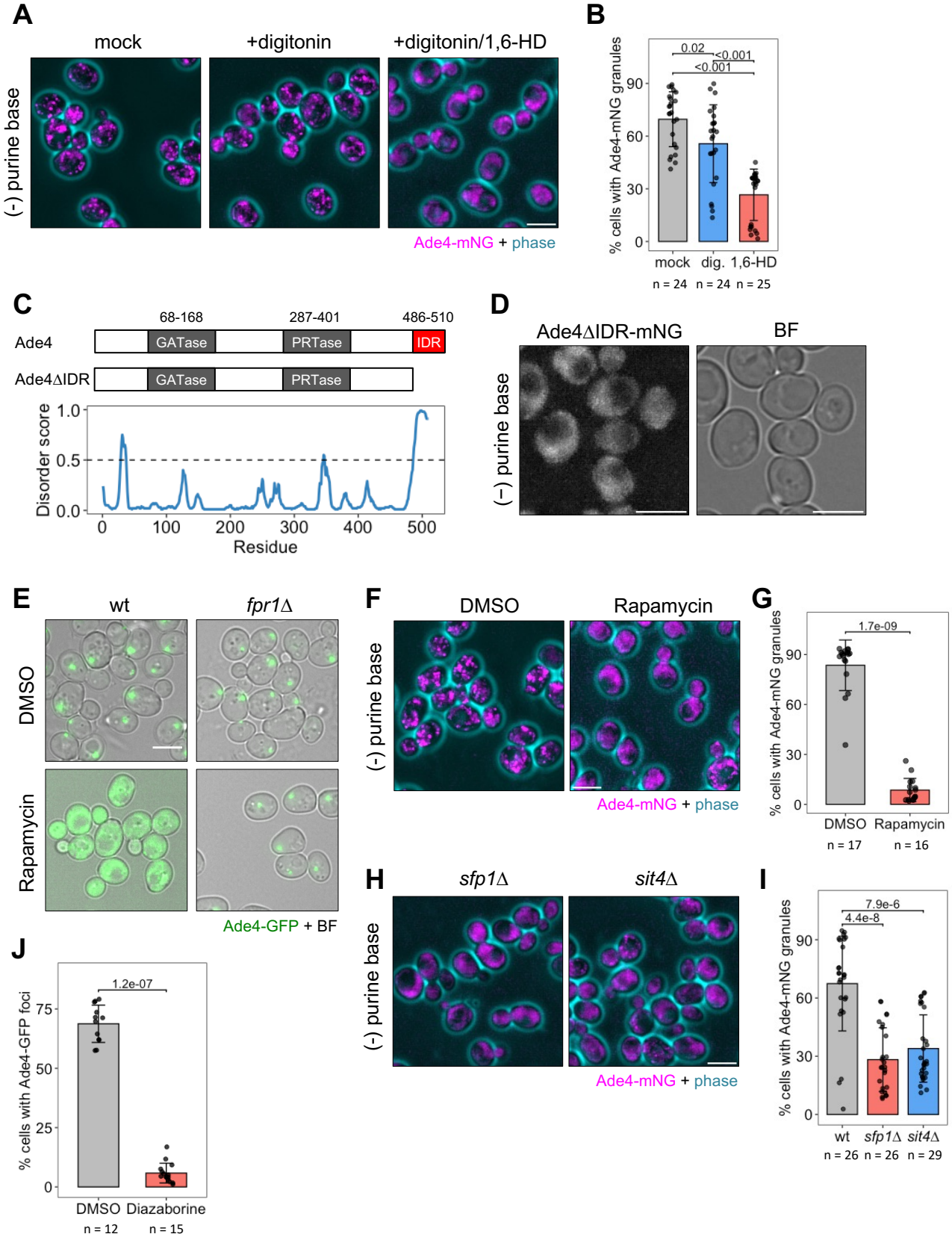

Figure S2: The IDR is conserved in PPATs of various species

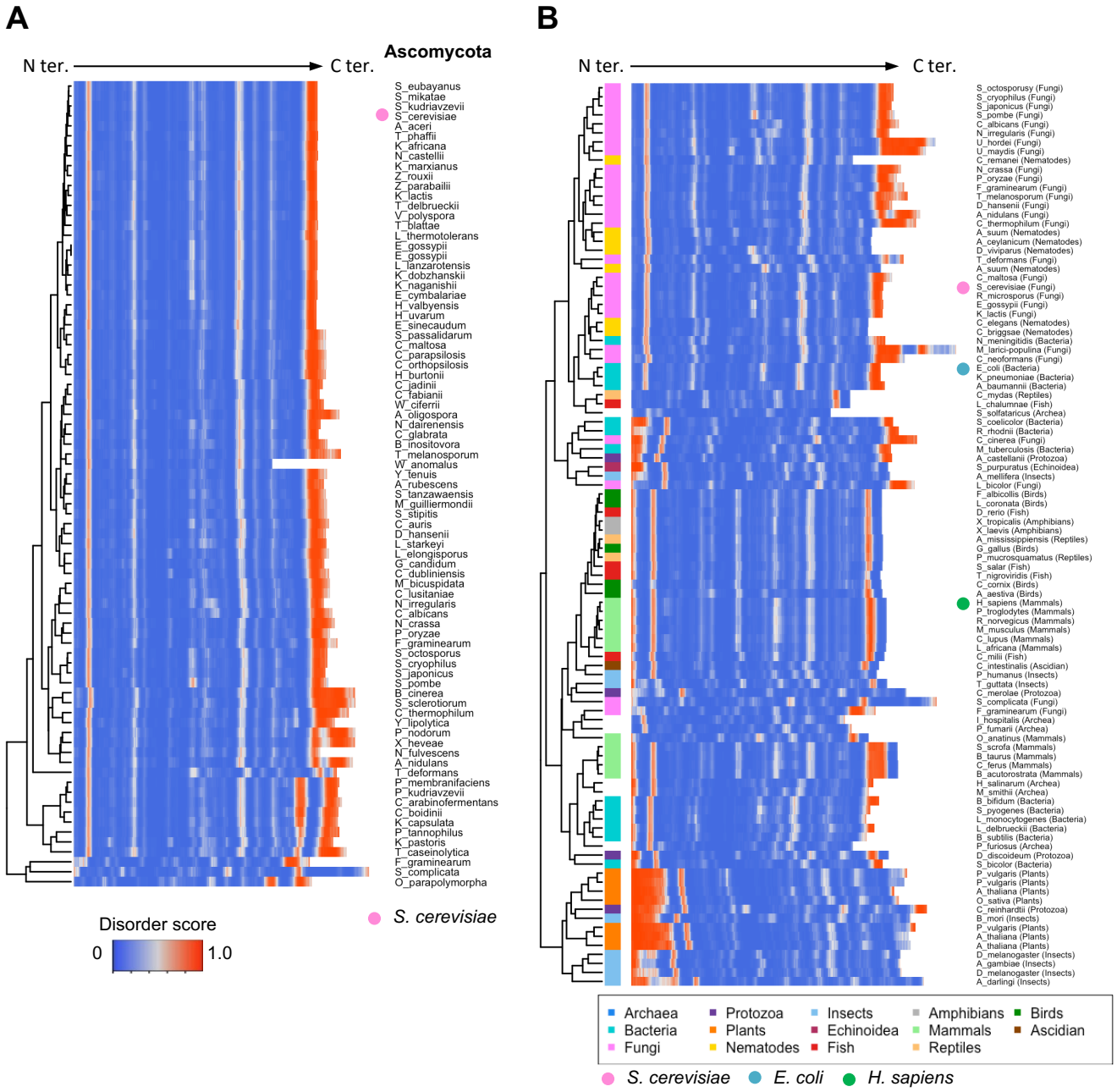

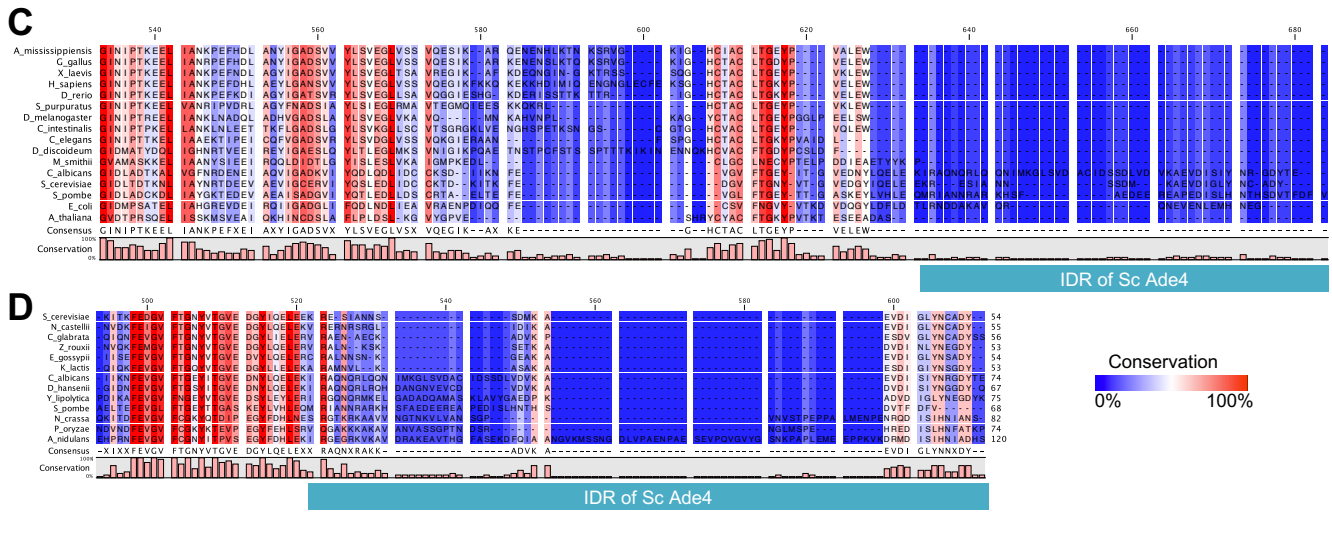

Figure S3: Formation of Ade4 condensates in TORC1-related mutants. Related to Figure 2

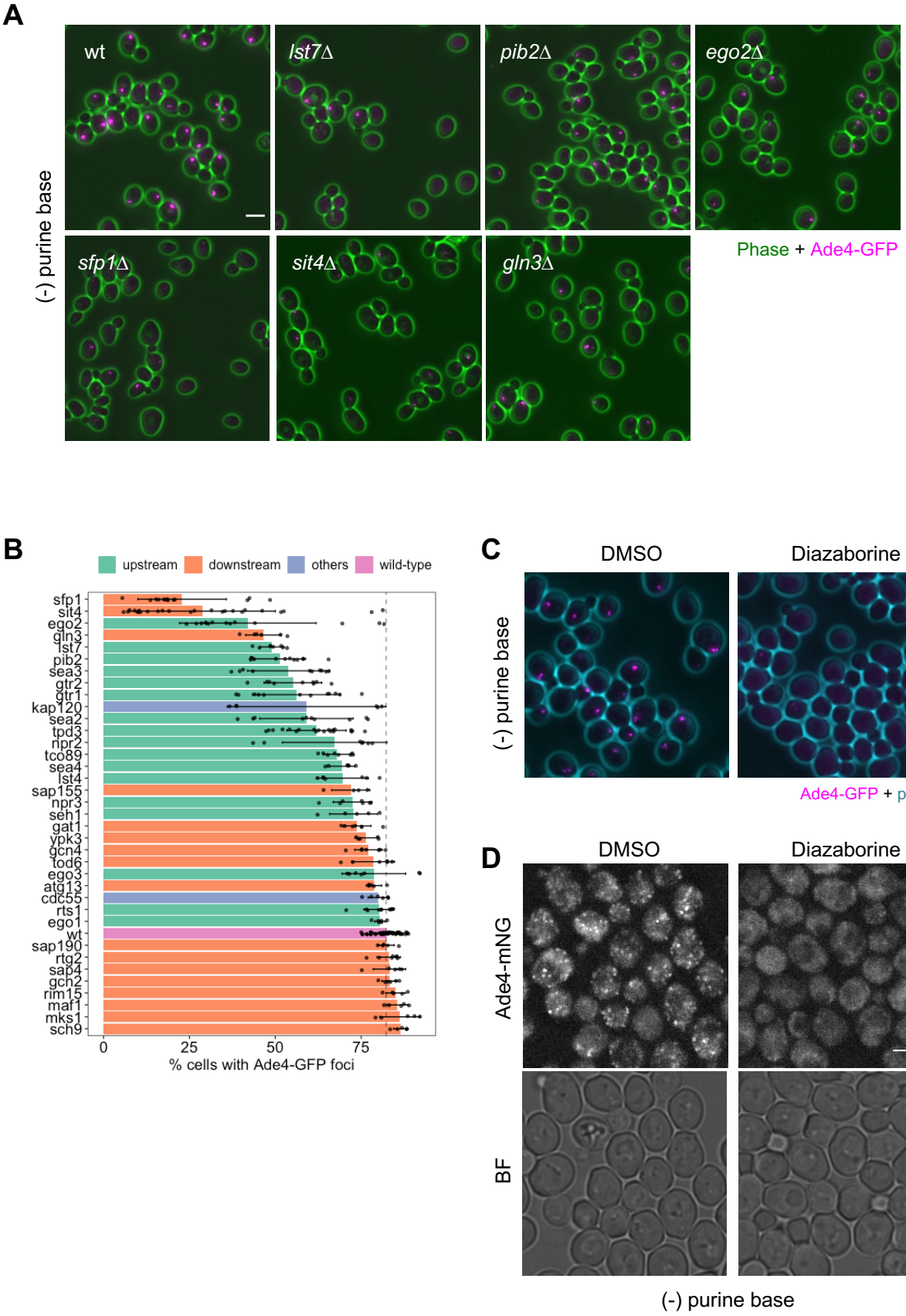

Figure 3: The Ade4 protein condensates into particles under molecular crowding conditions *in vitro*

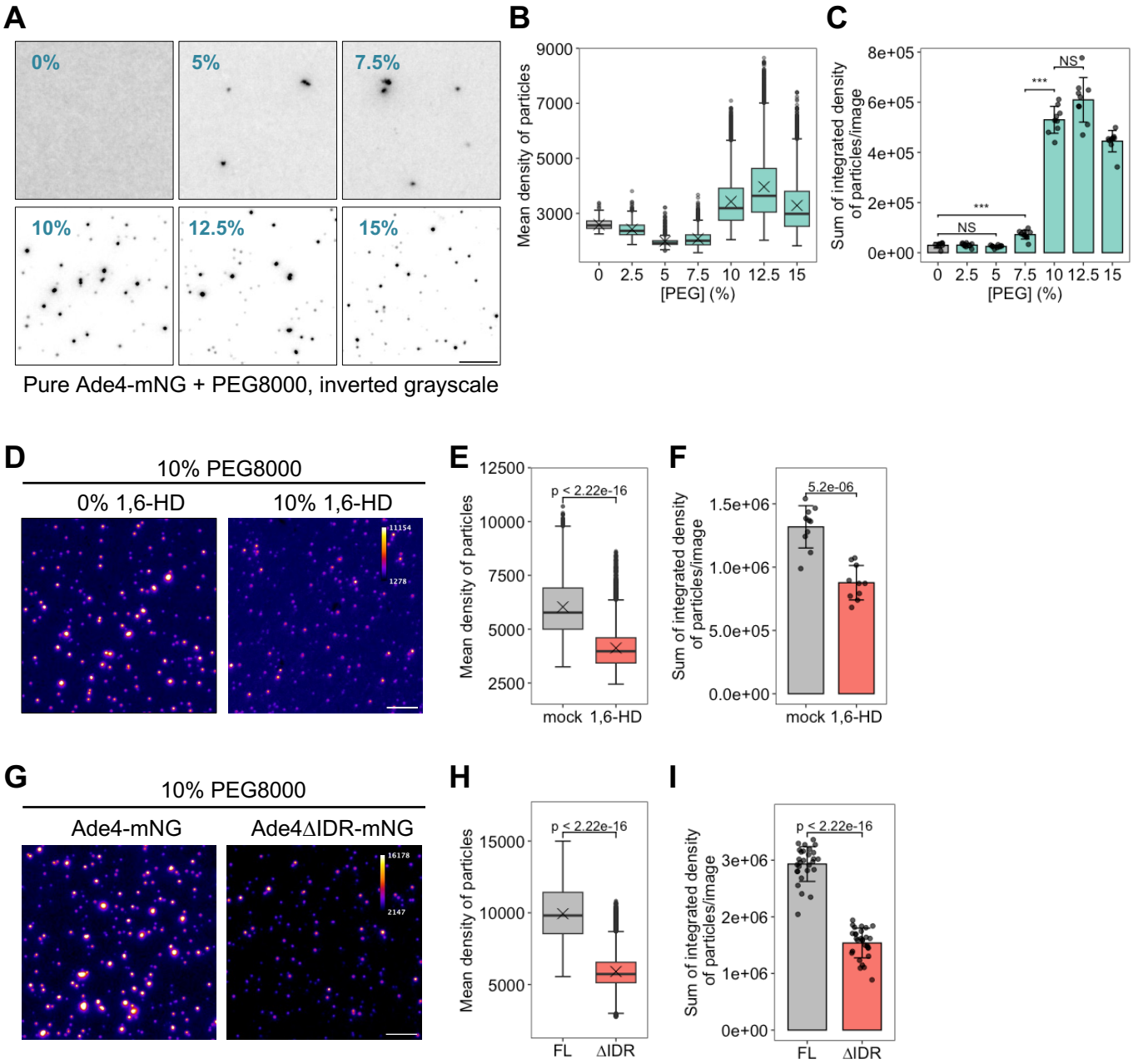

Figure S4: Purification and basic characterization of the Ade4 protein *in vitro*

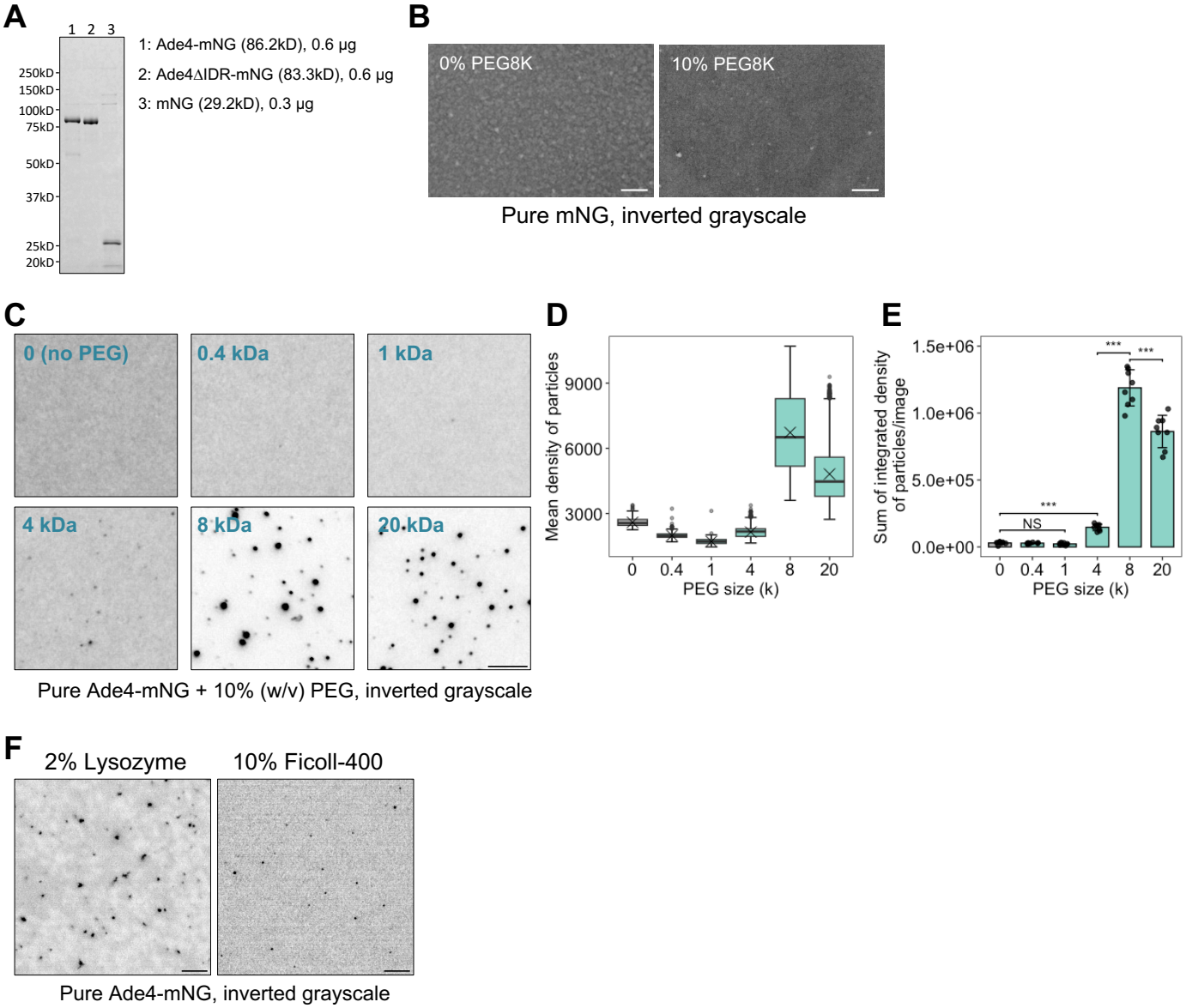

Figure S5: Estimation of the intracellular concentration of Ade4

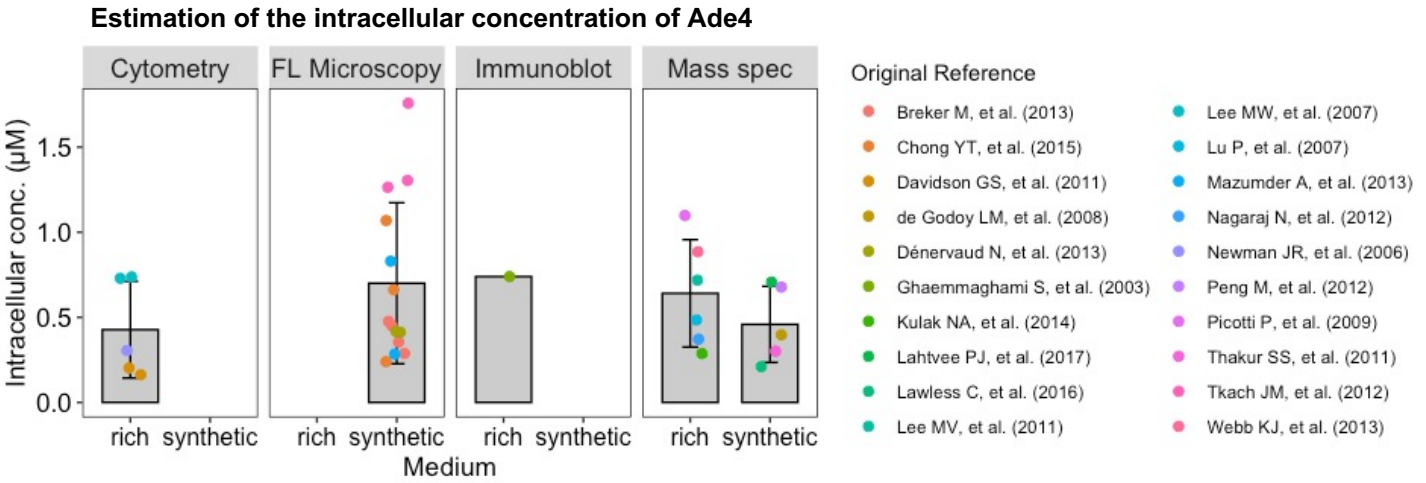

Figure 4: Metabolomics analysis of budding yeast cells grown in the absence and presence of adenine

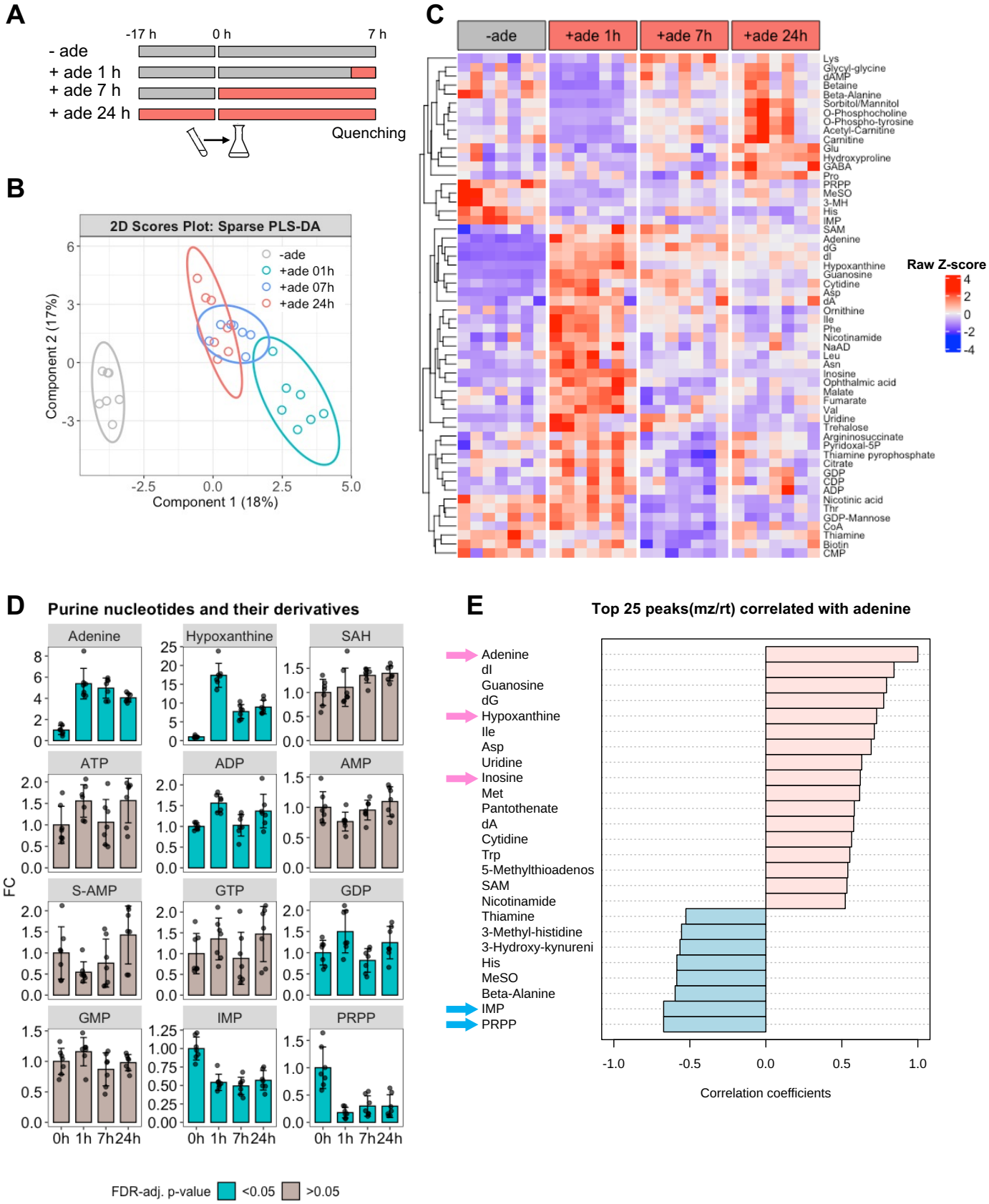

Figure S6: Additional data regarding the metabolomics analysis. Related to Figure 4

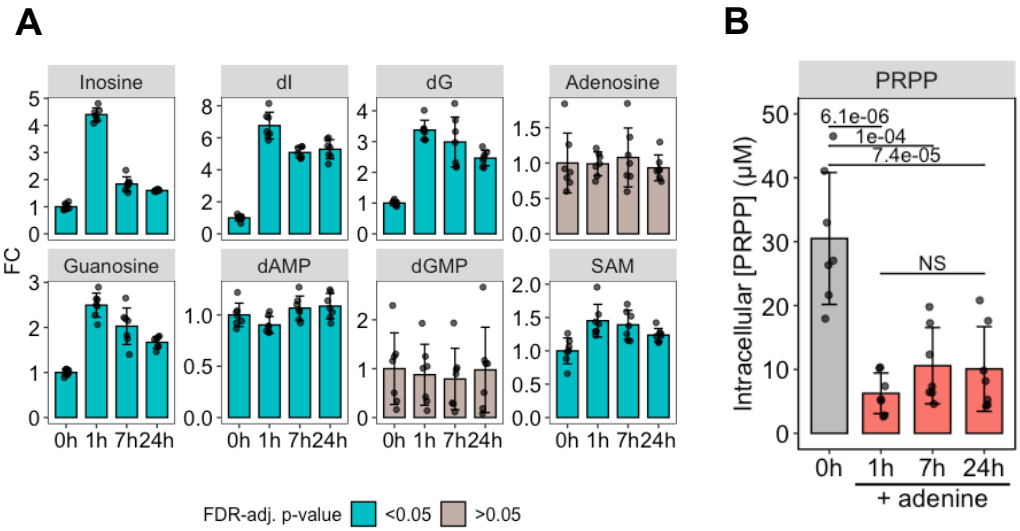

Figure 5: Intracellular derivatives of purine nucleotides regulate the formation of Ade4 condensates

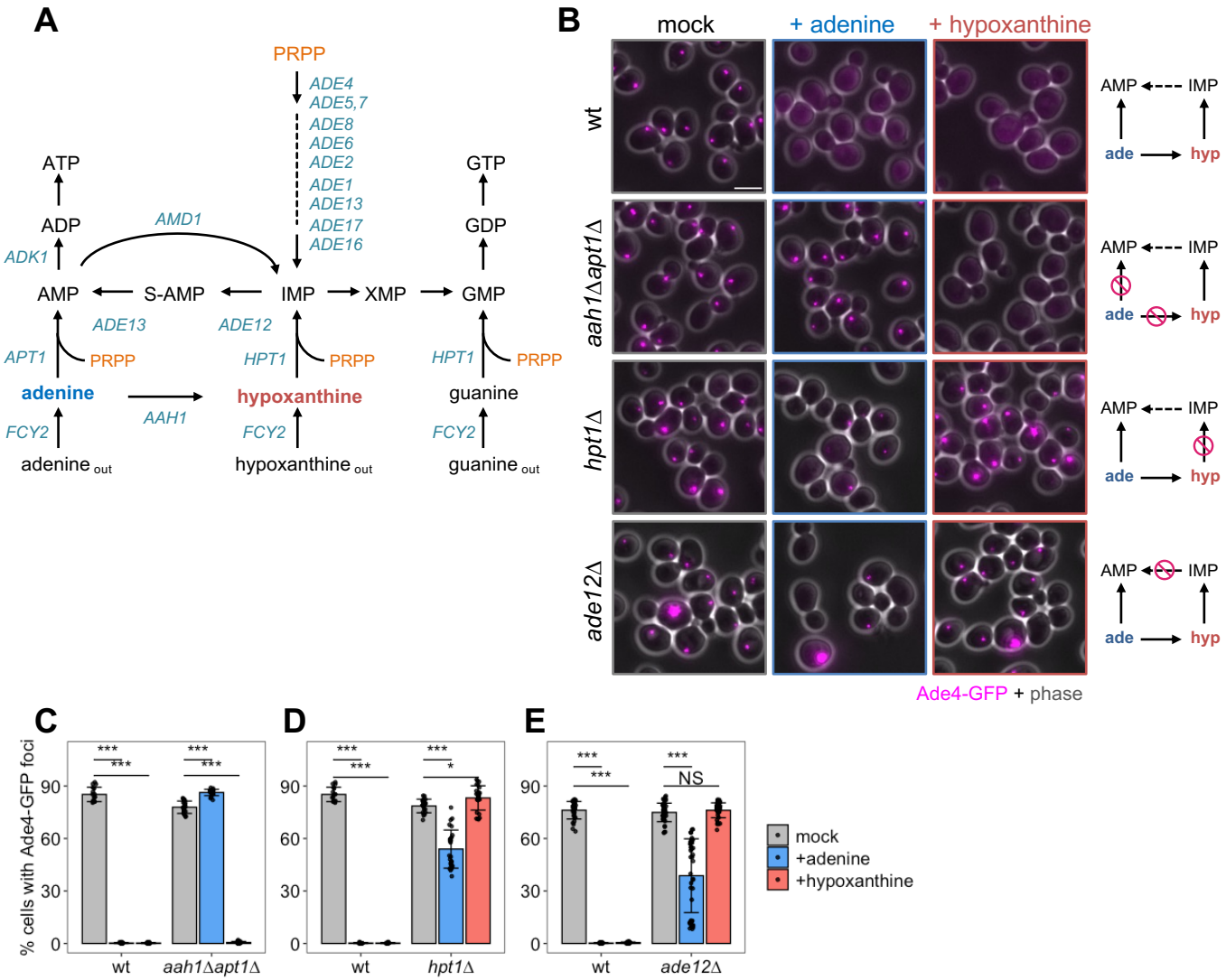

Figure S7: Alanosine inhibits the dissolution of the Ade4 foci in the presence of hypoxanthine

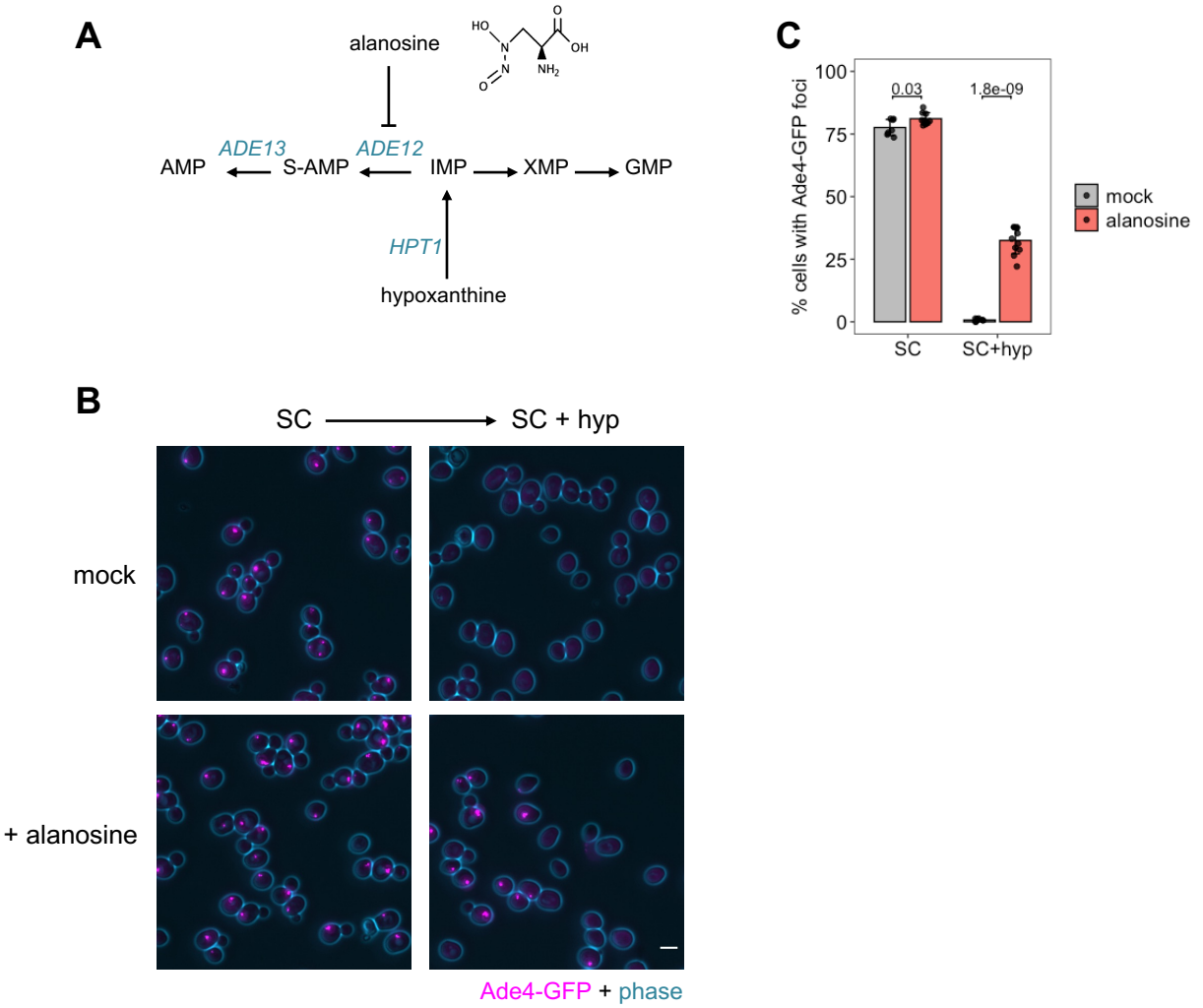

Figure 6: Purine nucleotides attenuate the assembly of the Ade4 condensates *in vitro*

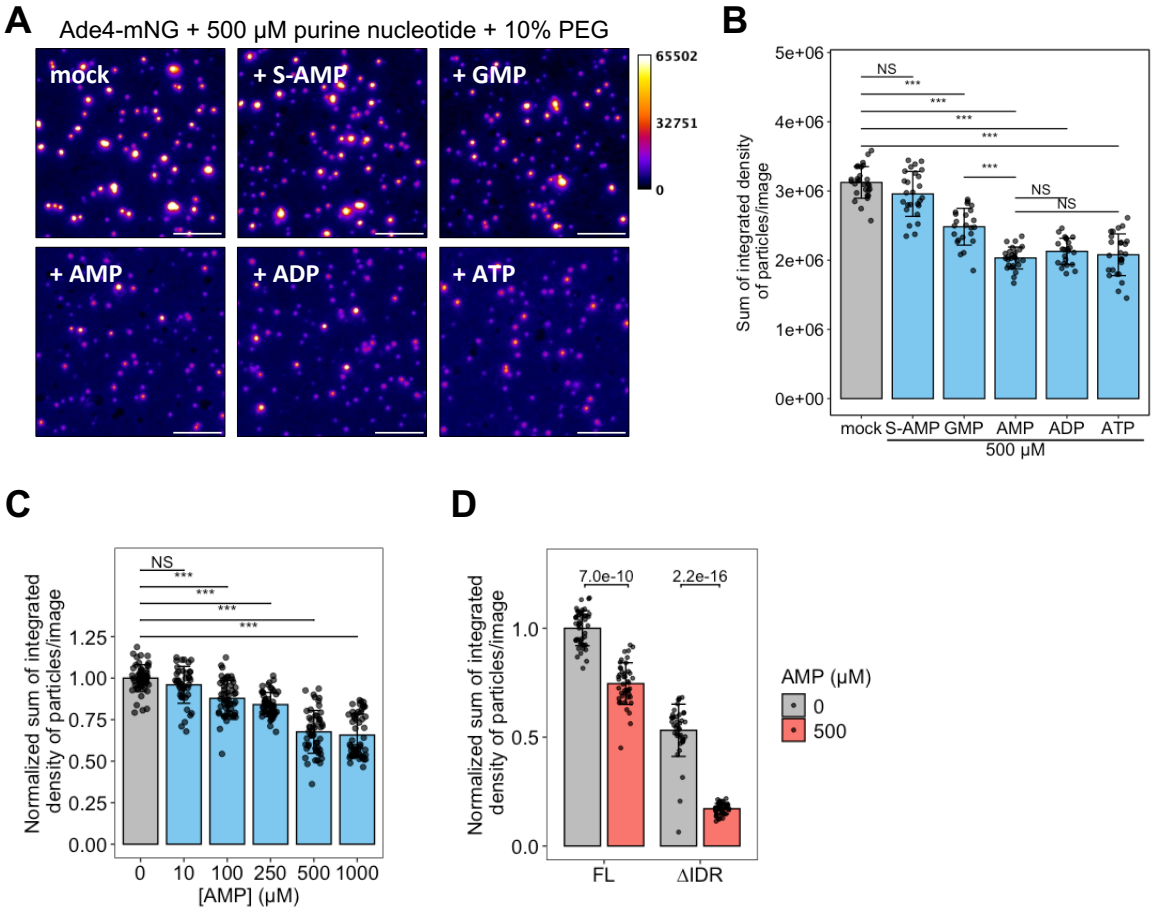

Figure S8: Additional data regarding the assembly of the Ade4 condensates *in vitro*, related to Figure 6

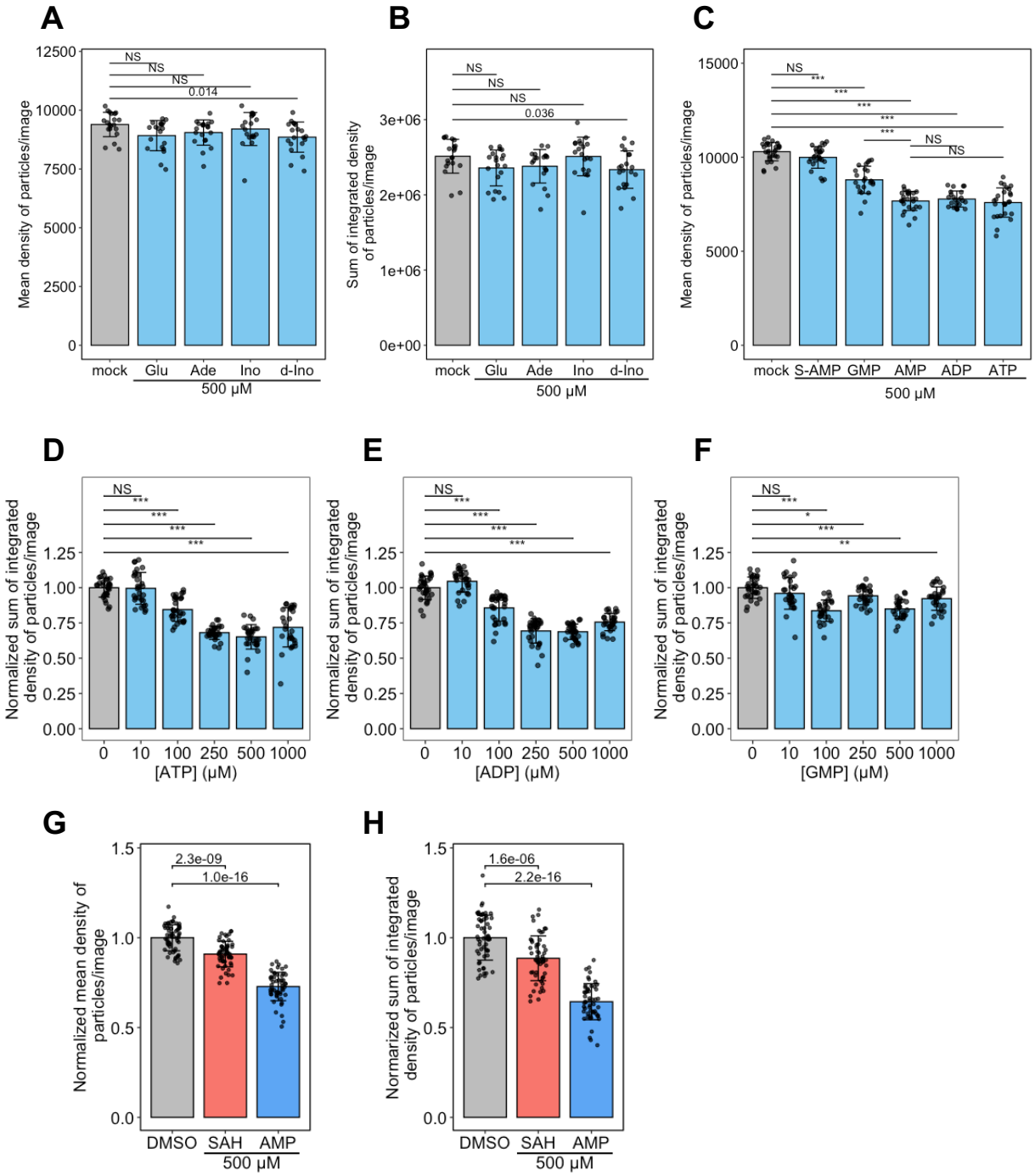

Figure S9: Effect of IMP on the assembly of Ade4 condensates *in vitro*

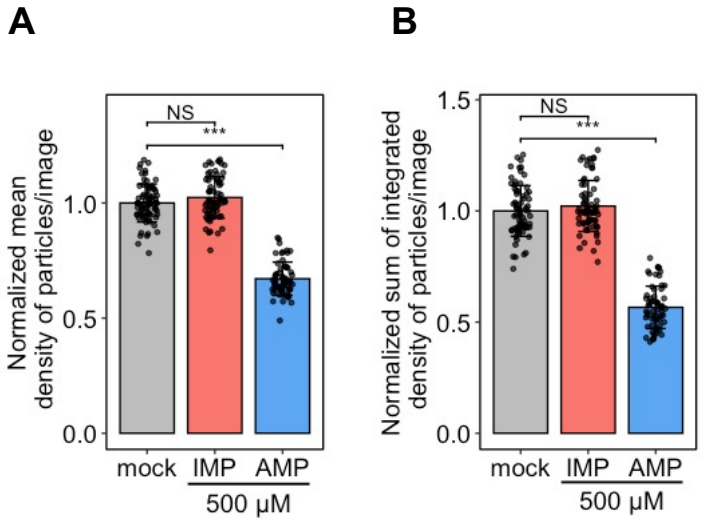

Figure 7: PRPP facilitates the assembly of the Ade4 condensates

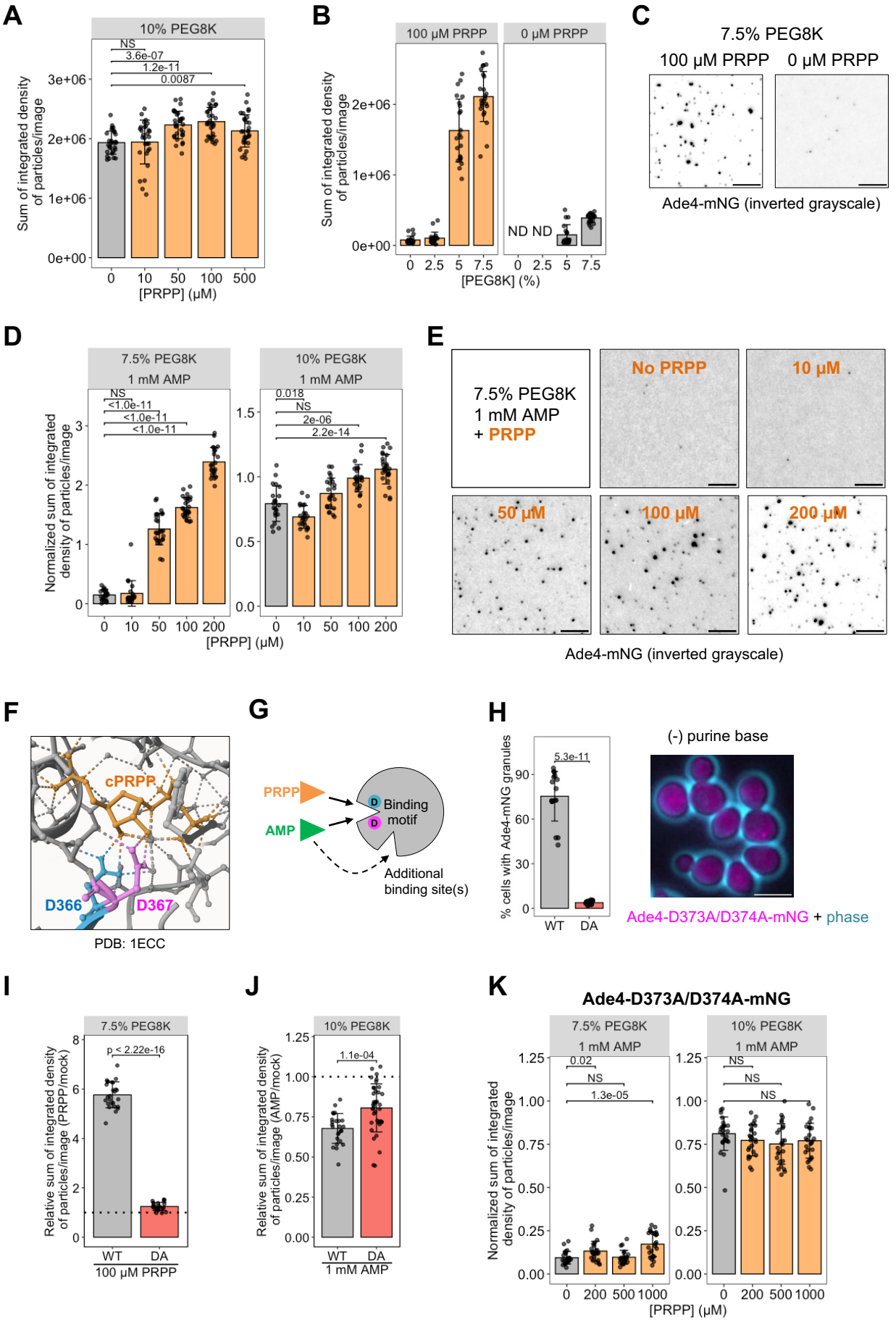

Figure S10: PRPP facilitates the assembly of the Ade4 condensates, related to Figure 7

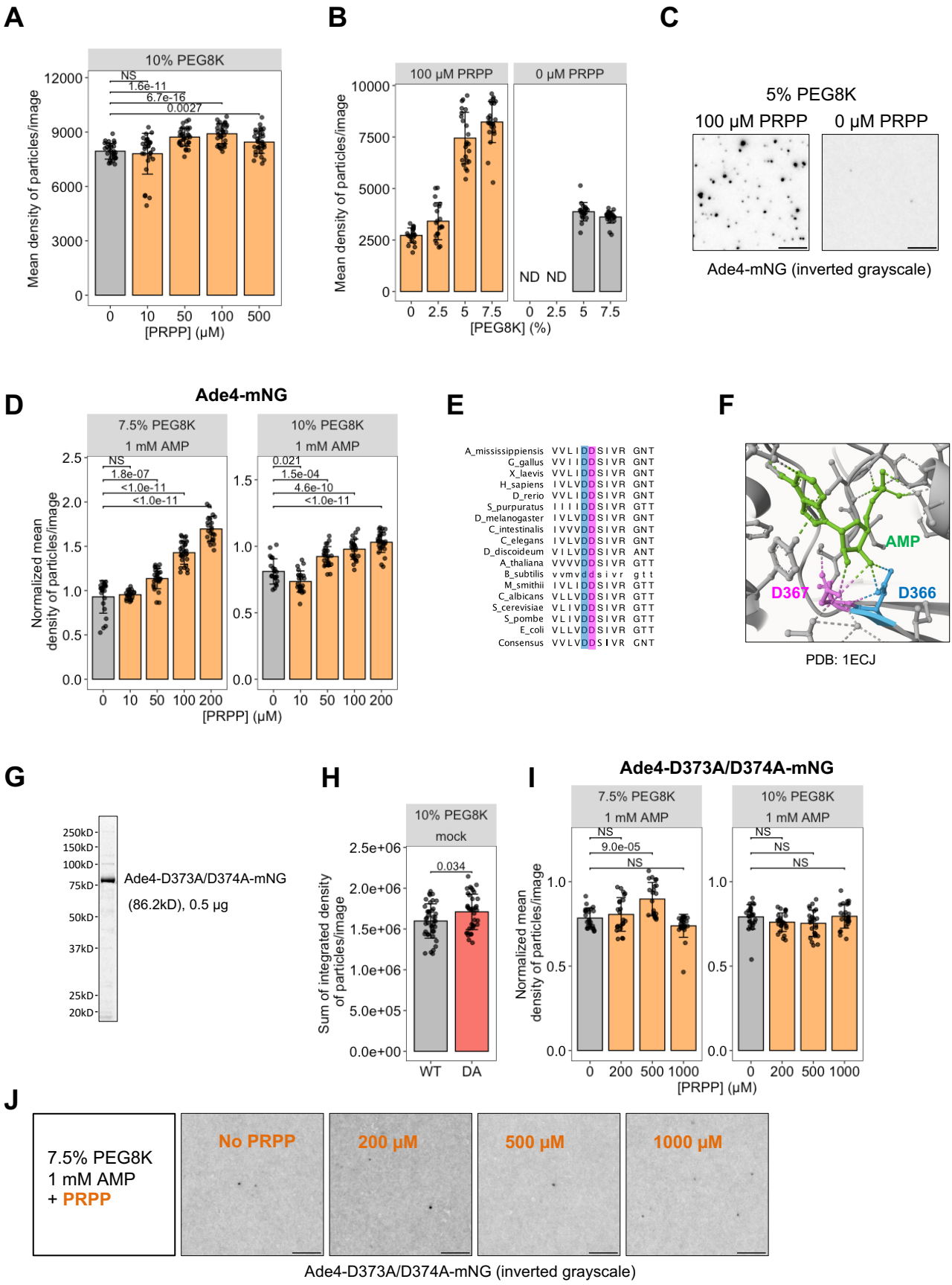

Figure 8: MD calculations predict the possible condensation-dependent activation of PPAT by enabling the intermolecular substrate channeling

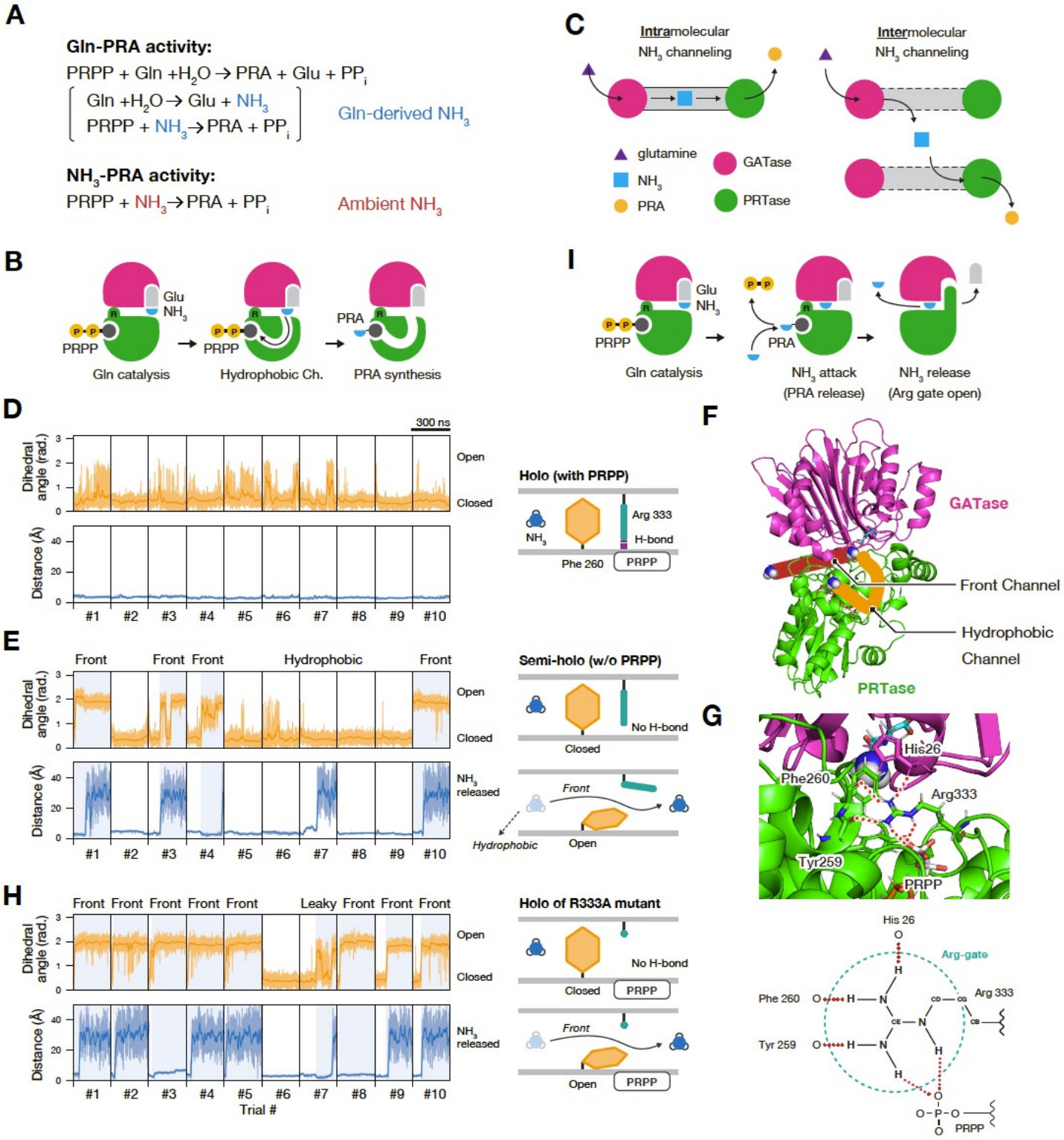

Figure S11: Possible enzymatic reaction pathway of PPAT

Figure 9: The formation of the Ade4 condensates is important for efficient *de novo* purine synthesis during cell growth

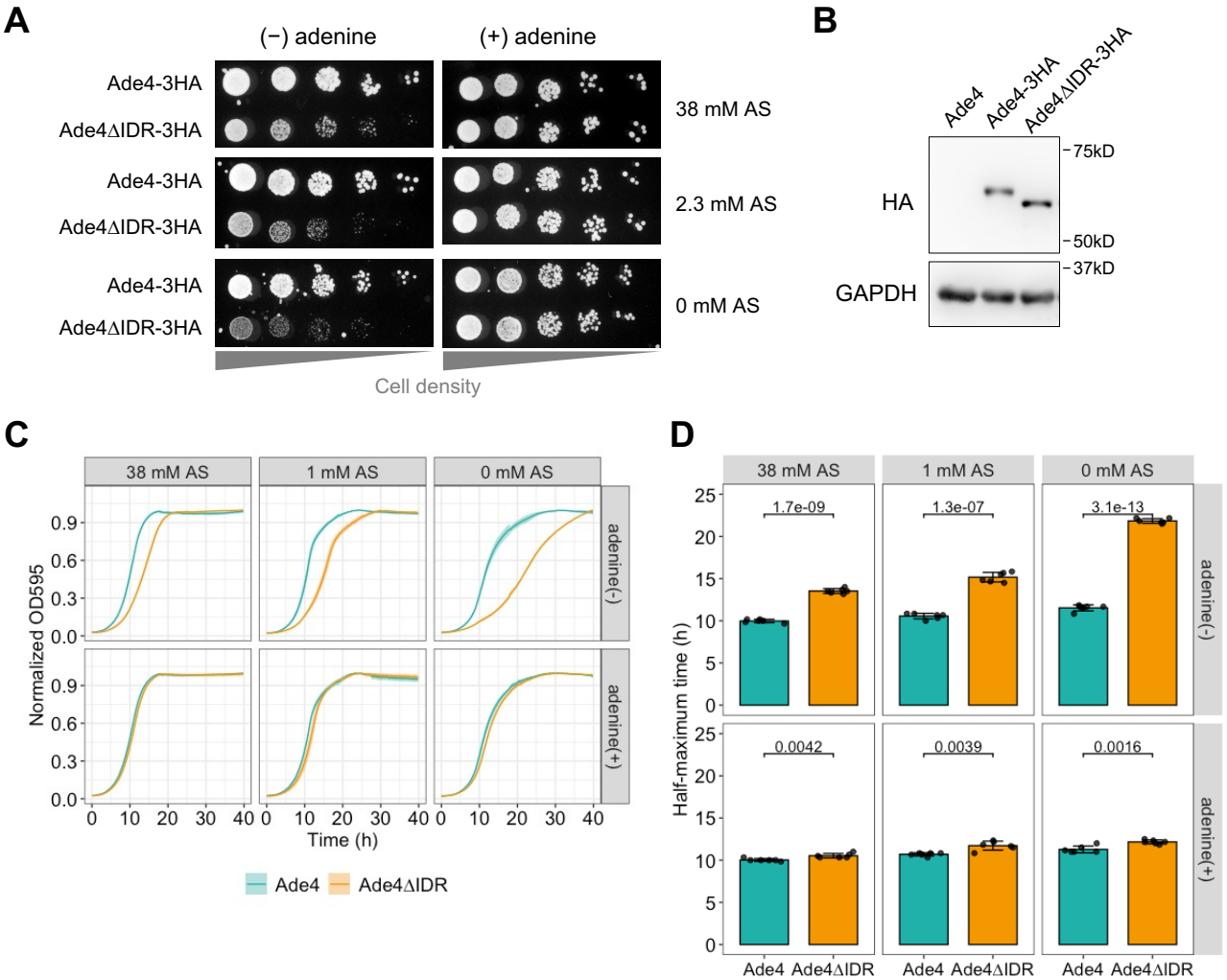
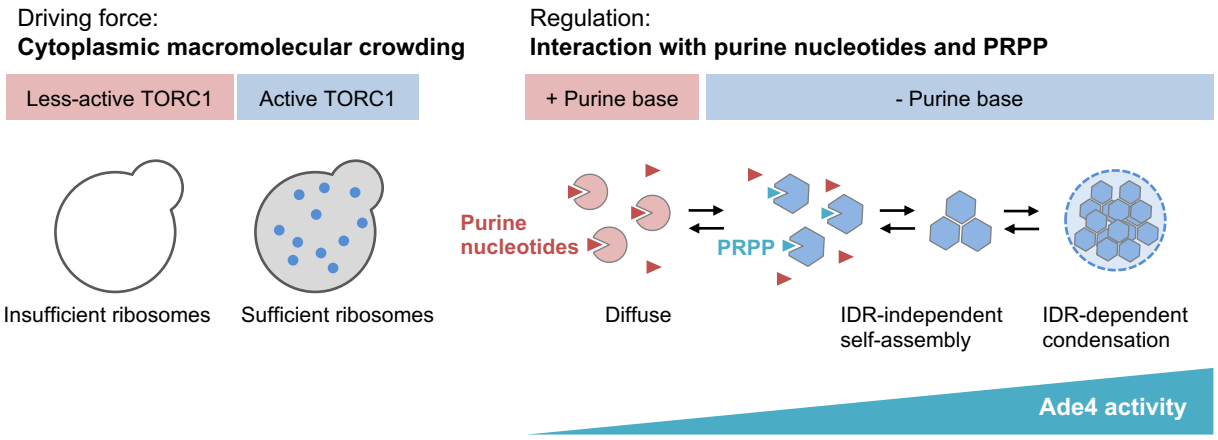
Figure 10: Molecular crowding and interactions with effectors regulate the Ade4 condensation